



On the shaping factors of the secondary microseismic wavefield

Lucia Gualtieri, Éléonore Stutzmann, Yann Capdeville, Véronique Farra,
Anne Mangeney, Andrea Morelli

► To cite this version:

Lucia Gualtieri, Éléonore Stutzmann, Yann Capdeville, Véronique Farra, Anne Mangeney, et al.. On the shaping factors of the secondary microseismic wavefield. *Journal of Geophysical Research: Solid Earth*, 2015, 120 (9), pp.6241-6262. 10.1002/2015JB012157 . insu-01400239

HAL Id: insu-01400239

<https://insu.hal.science/insu-01400239>

Submitted on 21 Nov 2016

HAL is a multi-disciplinary open access archive for the deposit and dissemination of scientific research documents, whether they are published or not. The documents may come from teaching and research institutions in France or abroad, or from public or private research centers.

L'archive ouverte pluridisciplinaire **HAL**, est destinée au dépôt et à la diffusion de documents scientifiques de niveau recherche, publiés ou non, émanant des établissements d'enseignement et de recherche français ou étrangers, des laboratoires publics ou privés.

Journal of Geophysical Research: Solid Earth

RESEARCH ARTICLE

10.1002/2015JB012157

Key Points:

- A mode conversion occurs moving from deep to shallow water and at the ocean-continent boundary
- Source contribution to land-recorded signals is strongly frequency dependent
- The amount of land-transmitted energy depends on the sediment thickness below the source region

Correspondence to:L. Gaultieri,
luciag@ldeo.columbia.edu**Citation:**Gaultieri, L., E. Stutzmann, Y. Capdeville, V. Farra, A. Mangeney, and A. Morelli (2015), On the shaping factors of the secondary microseismic wavefield, *J. Geophys. Res. Solid Earth*, 120, 6241–6262, doi:10.1002/2015JB012157.

Received 24 APR 2015

Accepted 28 JUL 2015

Accepted article online 4 AUG 2015

Published online 8 SEP 2015

On the shaping factors of the secondary microseismic wavefield

L. Gaultieri^{1,2}, E. Stutzmann¹, Y. Capdeville³, V. Farra¹, A. Mangeney^{1,4,5}, and A. Morelli⁶

¹Institut de Physique du Globe de Paris, Sorbonne Paris Cité, UMR 7154 CNRS, Paris, France, ²Now at Lamont-Doherty Earth Observatory, Columbia University, Palisades, New York, USA, ³Laboratoire de Planétologie et Géodynamique de Nantes, CNRS, Université de Nantes, UMR-6112, Paris, France, ⁴Université Paris Diderot, UMR 7154 CNRS, Paris, France, ⁵ANGE team, INRIA, CETMEF, Laboratoire Jacques Louis Lions, Paris, France, ⁶Istituto Nazionale di Geofisica e Vulcanologia, Bologna, Italy

Abstract Seismic noise in the period band 3–10 s is known as secondary microseism, and it is generated at the ocean surface by the interaction of ocean gravity waves coming from nearly opposite directions. In this paper, we investigate the seismic content of the wavefield generated by a source at the ocean surface and three of the major wavefield shaping factors using the 2-D spectral element method: the ocean-continent boundary, the source site effect, and the thickness of seafloor sediments. The seismic wavefield recorded on the vertical component seismograms below the seafloor is mainly composed of the fundamental mode and the first overtone of Rayleigh waves. A mode conversion from the first overtone to the fundamental mode of Rayleigh waves occurs at the ocean-continent boundary. The presence of a continental shelf at the ocean-continent boundary produces a negligible effect on land-recorded seismograms, whereas the source site effect, i.e., the source location with respect to the local ocean depth and sediment thickness, plays the major role. A source in shallow water mostly enhances the fundamental mode of Rayleigh waves, whereas a source in deep water mainly enhances the first overtone of Rayleigh waves. Land-recorded long-period signals ($T > 6$ s) are mostly due to deep water sources, whereas land-recorded short-period signals ($T < 6$ s) are due to sources in relatively shallow water, located close to the shelf break. Seafloor sediments around the source region trap seismic waves reducing the amplitude of land-recorded signals, especially at long periods ($T > 6$ s).

1. Introduction

Seismic noise is the continuous oscillation of the Earth recorded worldwide, in response to the interaction among atmosphere, ocean, and solid Earth. The strongest ambient noise signal is known as microseismic noise and its spectrum is typically dominated by two main peaks with periods of about 7 s and 14 s. The smallest of these two peaks, which falls in the period band between 10 s and 20 s, is called primary microseisms, while the largest one, between about 3 s and 10 s, is called secondary microseisms (for a review on seismic noise, the reader is addressed to, e.g., Webb [1998]).

In this study, we deal with the secondary microseismic noise which is generated by the nonlinear interaction of ocean waves coming from opposite directions, driven by wind and whose restoring force is gravity [Longuet-Higgins, 1950; Hasselmann, 1963]. The nonlinear interaction among ocean gravity waves generates seismic noise with a frequency equal to the sum of ocean wave frequencies.

In the ocean, gravity primarily affects the pressure field in a close-to-surface layer, whose thickness is comparable with the wavelength of ocean gravity waves, whereas compressibility—i.e., seismic P waves—has a dominant effect on the pressure field in the remaining part of the ocean [Longuet-Higgins, 1950]. Since the wavelength of ocean gravity waves at these periods ($T = 3$ –10 s) is significantly smaller than the ocean depths—tens or hundreds of meters versus thousands of meters, with the exception of coastal regions—secondary microseismic noise sources are located at the upper surface of the ocean or just below it.

A noise source generates acoustic or P waves which are multiply reflected inside the ocean and converted to elastic body waves at the seafloor [Gaultieri *et al.*, 2014]. Elastic P and S waves, in turns, interact constructively below the seafloor and generate surface waves. The wavefield below the seafloor is modulated by the multiple reflections of P waves in the liquid layer, which has been previously called ocean site effect [e.g., Longuet-Higgins, 1950; Arduin and Herbers, 2013; Gaultieri *et al.*, 2013, 2014].

Since microseismic noise is generated in oceanic environments, undersea measurements are usually much noisier than land observations [e.g., Webb, 1998, 2002]. Moreover, it has been shown that the seismic noise level differs from ocean to ocean, which may depend on storm activity and seafloor configuration. For example, the vertical component of noise spectrum recorded at North Atlantic sites [e.g., Beauduin and Montagner, 1996] is characterized by a smaller amplitude than the vertical component of noise spectrum recorded at Pacific sites [e.g., Collins *et al.*, 2001].

The amplitude of land-recorded seismic noise in relation with the source location and efficiency to transmit seismic energy from the ocean to the continent is still under debate. Evidence of dominant offshore noise sources located in deep ocean environments has been documented by Webb and Constable [1986], Cessaro [1994], Stehly *et al.* [2006], Kedar *et al.* [2008], and Obrebski *et al.* [2012] for noise Rayleigh waves and by Gerstoft *et al.* [2008], Koper and de Foy [2008], Koper *et al.* [2009, 2010], Zhang *et al.* [2010], Obrebski *et al.* [2013], and Gaultieri *et al.* [2014] for noise body waves. Evidence of noise sources associated with coastal reflection in shallow water has been documented by Derbyshire [1992], Bromirski *et al.* [1999], Bromirski [2001], Bromirski and Duennbier [2002], Bromirski *et al.* [2005], Essen *et al.* [2003], Schulte-Pelkum *et al.* [2004], Gerstoft and Tanimoto [2007], Tanimoto [2007], Yang and Ritzwoller [2008], and Arduin *et al.* [2012]. Evidence of both of them has been found by Haubrich and McCamy [1969], Friedrich *et al.* [1998], Chevrot *et al.* [2007], Stutzmann *et al.* [2012], and Bromirski *et al.* [2013].

Recently, Lin *et al.* [2014] have shown that land stations located on opposite sides of Taiwan island record a very different noise level. They claim that the different shape and steepness of the ocean-continent boundary on both sides of Taiwan may play an important role in reflection and transmission of microseismic waves coming from the ocean.

Ying *et al.* [2014] recently modeled the seismic wavefield generated by a vertical force located below the seafloor in a realistic 2-D Earth model, which includes a thick layer of seafloor sediments. In their modeling, the land-recorded signal generated by an offshore source located below the seafloor, inside the sedimentary layer, is weak. Nevertheless, their source location does not correspond to the location of a secondary microseismic source, which has to be considered at the surface of the ocean and not below the seafloor (see Appendix B for a comparison between the modeling in both cases).

Recent studies based on the cross-correlation analysis of ocean bottom records have shown several features of the seismic wavefield recorded at the ocean bottom [e.g., Harmon *et al.*, 2007; Yao *et al.*, 2011; Harmon *et al.*, 2012; Takeo *et al.*, 2013, 2014; Tian and Ritzwoller, 2015]. In particular, it has been seen that the fundamental mode of Rayleigh waves is always present on the vertical component of ocean bottom noise records with periods between 3 and 10 s, whereas the first overtone appears only at short periods [Harmon *et al.*, 2007; Yao *et al.*, 2011]. Several studies have also shown the presence of a slow phase having group velocity around 1 km/s [Press and Ewing, 1948; Press *et al.*, 1950; Ewing *et al.*, 1957; Oliver and Ewing, 1958; Ritzwoller and Levshin, 2002; Harmon *et al.*, 2012; Tian and Ritzwoller, 2015].

In order to evaluate the effect of the ocean-continent boundary, the ocean depth under the source and the seafloor sedimentary layer, we model the seismic wavefield generated by a single source at the ocean surface. The employment of a single source allows us to simplify the problem and investigate the wavefield content. Moreover, the full knowledge of the wavefield generated by a single source is a fundamental step forward in understanding signals generated by extended pressure sources. We use the 2-D spectral element method, detailed in section 2. Two different realistic seafloor profiles, including their respective ocean-continent boundaries—taken in France and in California (U.S.)—have been used in order to compute the seismic wavefield recorded on oceanic and land stations (see sections 2 and 3). We compare oceanic and continental ground velocity vertical component seismograms and spectra generated by a source located offshore, in a deep water environment and by a source located close to the continental shelf (section 4). Finally, the effect of a seafloor sedimentary layer on synthetic seismograms and spectra is shown in section 5 for a varying source location. A summary of our main results and a comparison with previous studies is shown in section 6.

2. Method and Model Setup

In order to model the seismic wavefield generated by a source at the ocean surface, we adopt the spectral element method, which handles solid-fluid domain decomposition and allows the introduction of irregular

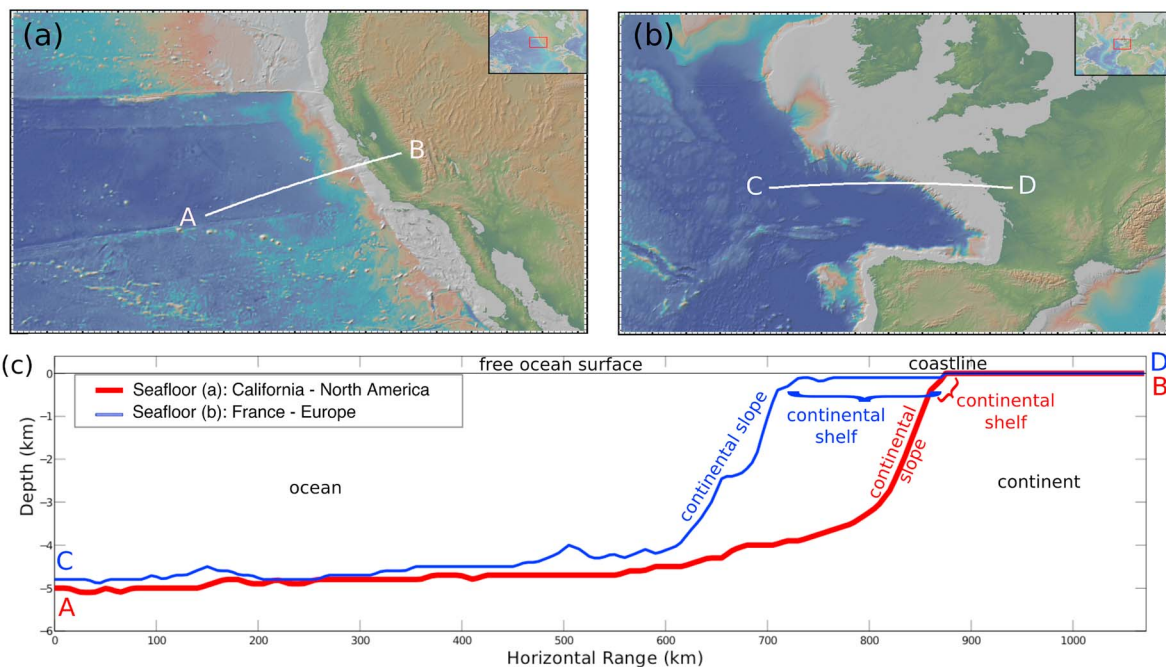


Figure 1. (a) Map of the bathymetry around the profile AB (California), where A is taken at (131°W; 33.7°N) and B at (120°W; 37.1°N). (b) Map of the bathymetry around the profile CD (France), where C is taken at (15°W; 47°N) and D at (0.5°W; 47°N). (c) Seafloor topographies along the profiles AB (in red) and CD (in blue).

discontinuities, such as the seafloor topography (for reviews on the spectral element method the reader is addressed to, e.g., Komatitsch *et al.* [2005] and Chaljub *et al.* [2007]).

In order to simplify the problem, we restrict our computations in two dimensions. In fact, with respect to the 3-D case, the 2-D spectral element method yields faster quantitative estimations and the mesh configuration can be easily handled. One of the major differences between the 3-D and the 2-D wave propagation concerns the geometrical spreading, which is equal to 1 in 2-D for surface waves. Moreover, the employment of the 2-D wave propagation prevents to account for the coupling between Rayleigh and Love waves.

A 2-D regional Earth model is employed and absorbing boundaries are used to avoid parasitic reflections from the sides [Festa and Vilotte, 2005]. The upper surface of the liquid layer is a free surface where the pressure is enforced to zero.

The mesh configuration has been adapted to follow two bathymetric profiles, whose locations are shown in Figures 1a and 1b, respectively. In Figure 1c, the two bathymetric profiles are compared. The seafloor profile AB (in red) is taken on the U.S. West Coast between A = (131°W, 33.7°N) and B = (120°W, 37.1°N), whereas the seafloor profile CD (in blue) is taken in France, in the Gulf of Biscay, between C = (15°W, 47°N), and D = (0.5°W, 47°N). Hereafter, we refer to models a and b for California and Gulf of Biscay models, respectively, as denoted in Figure 1c.

In both cases, the coastline is located at $x = 885$ km along the horizontal range. The continental shelf break is located at $x = 875$ km and $x = 710$ km in models a and b, respectively. In both cases, the continent is located on the right side of the profile and it extends up to 200 km away from the coastline. No topography is considered on the continent and the free surface condition is applied everywhere. On the left side of Figure 1c, the abyssal plain reaches about 5 km depth in both cases. Both profiles are characterized by a rough abyssal plain and similar continental slope down to about 3 km. At deeper ocean, the steepness of the two bathymetries differs before reaching the abyssal plain.

The main difference between these bathymetric profiles is the horizontal size of the continental shelf. The continental shelf is the underwater landmass between the coast and the continental slope, characterized by very shallow water (about 400 m in our cases). Model a is characterized by a very small continental shelf with a horizontal extension of about 10 km. The continental shelf of model b is about 170 km long. The digital

bathymetries in Figure 1 have been taken from *Ryan et al.* [2009] and *Haxby et al.* [2010], freely available at www.geomapapp.org. Bathymetries have resolutions as high as 50 m where high-resolution data exist.

In order to investigate separately the effect of the ocean-continent slope, the effect of the ocean depth under the source and the effect of seafloor sediments on the seismic wavefield, the same elastic properties have been used for both models. The ocean layer is characterized by P wave velocity $\alpha_w = 1.5$ km/s and density $\rho_w = 1.0$ g/cm³. The crust is defined by P wave velocity $\alpha_c = 5.8$ km/s, S wave velocity $\beta_c = 3.2$ km/s, and density $\rho_c = 3$ g/cm³, whereas the sedimentary layer by P wave velocity $\alpha_s = 2$ km/s, S wave velocity $\beta_s = 0.8$ km/s, and density $\rho_s = 1.7$ g/cm³. Seismic attenuation is not taken into account, since attenuation is hardly known at these frequencies. We have verified that deeper structures, such as the Earth's mantle, do not affect our results. In particular, we have checked that the main observed features due to the fundamental mode and the first overtone of Rayleigh waves are not affected by a multilayered mantle structure at periods between 3 and 10 s and that the presence of higher modes does not modify the shape of seismograms and spectra.

A pressure source is located 1 m below the free ocean surface. In the frequency domain, the source wavelet is flat between 0.1 and 0.3 Hz and decays as a cosine on both sides up to 0.05 Hz and 0.35 Hz, respectively. Simulated traces have been filtered in the secondary microseismic frequency band, i.e., between 0.1 and 0.3 Hz, in order to avoid the effect of the source wavelet borders. The source central time is set to 40 s. A set of receivers is placed 1 m below the seafloor, in the solid Earth, following the seafloor profiles in Figure 1c and in the continent, 1 m below the free surface.

For each mesh element, a Lagrange polynomial of degree 5 has been used. The size of each element in which the physical domain has been decomposed is constrained by the shortest wavelength propagated in the medium and by the chosen polynomial order [e.g., *Cupillard et al.*, 2012]. As a consequence, we choose the element size to be 2.5 km for simulations without sediments and 1.5 km for simulations with sediments. To ensure the stability of the time marching, the time step of the finite-difference scheme is 0.0005 s for all simulations, in order to verify the Courant-Friedrichs-Lowy condition [*Courant et al.*, 1928].

3. The Ocean-Continent Boundary Effect

Let us consider a source located at $x = 600$ km and $x = 430$ km in models a and b, respectively. The distance between the source and the coastline is 285 km in model a and 455 km in model b because of the different horizontal extension of the continental shelf, much longer in France than in California (see previous section). In both cases, the source is located in a deep ocean environment.

Figure 2 displays the instantaneous energy (i.e., $v_x^2 + v_z^2$) of the seismic wavefield generated by the source (black star just below the ocean surface). Figures 2a and 2b refer to models a and b, respectively. The same normalization coefficient has been used for all snapshots.

The ocean acts as a waveguide, where acoustic P waves are multiply reflected between the ocean free surface and the seafloor. In the ocean layer, they interfere constructively and generate a strong energy packet which propagate away from the source with an apparent horizontal velocity of about 1 km/s. When the wavefield reaches the ocean-continent boundary ($t = 150$ s), part of the energy is transmitted to the continent and part is reflected back.

In Figure 2a, where the continental shelf is very narrow, the land-transmitted energy is weak and uniformly distributed along the continent ($t \geq 250$ s). In Figure 2b, where the continental shelf is longer than the previous case (170 km), the instantaneous energy is transmitted to the continent in well-defined energy packets ($t \geq 250$ s). In Figure 2b at $t = 300$ s, we observe the instantaneous energy transmitted to the continent and the energy reflected back from the ocean-continent boundary (signals within the blue ellipses at $t = 300$ s in Figure 2).

In order to study the seismic wavefield, a set of receivers is located 1 m below the modeled seafloor, as well as in the modeled continental region. In Figure 3, we present the vertical component of ground velocity synthetic seismograms recorded just below the seafloor (blue traces), along the ocean-continent boundary (red traces) and on land (black traces), considering both bathymetries. Figures 3a and 3b correspond to models a and b, respectively, as shown on the panels above the seismograms. Each colored dot, located just below the bathymetries, denotes a seismic station where the corresponding trace is recorded. Since we are interested in relative amplitudes, we normalize all seismograms by the same factor.

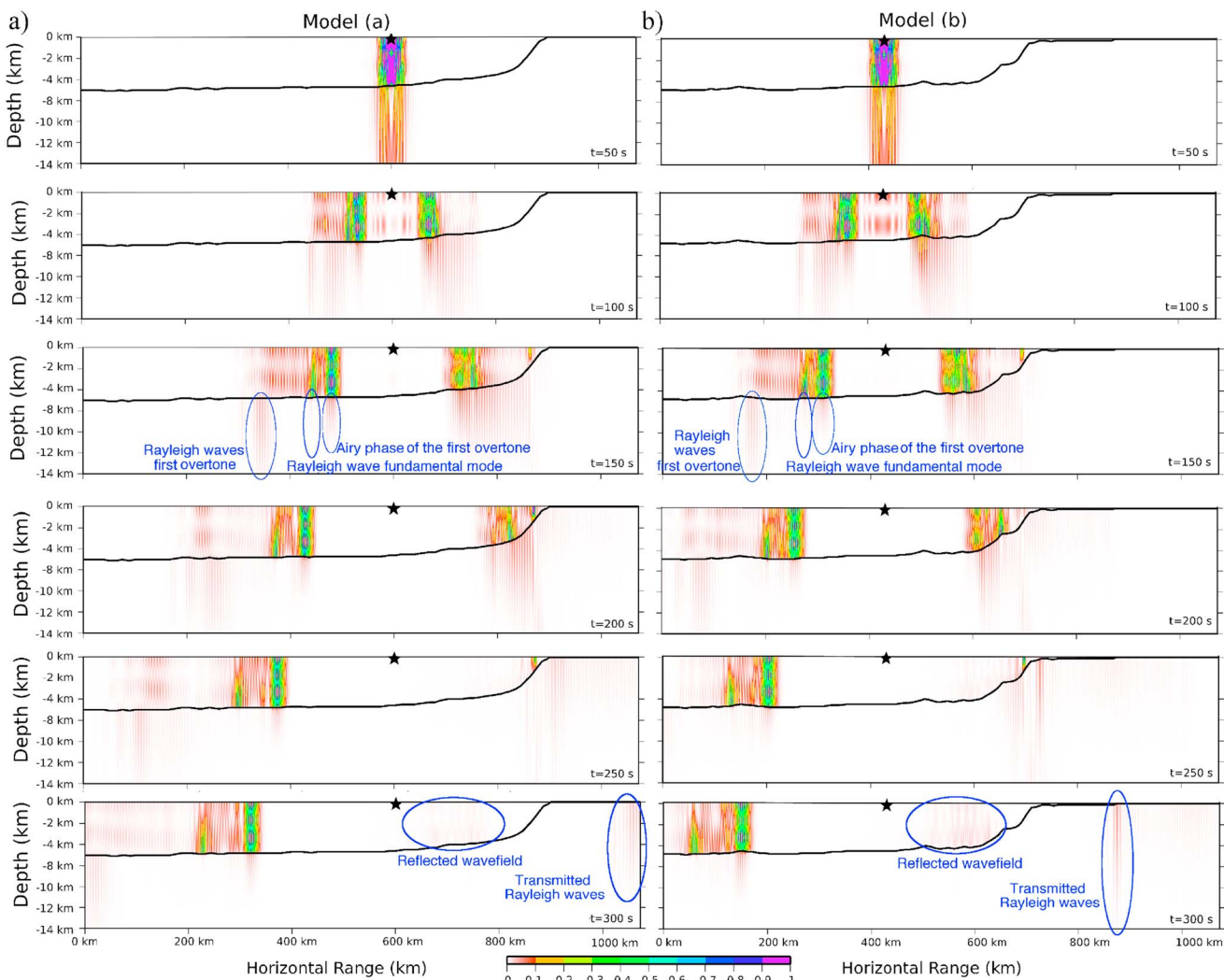


Figure 2. Instantaneous energy associated with the seismic wavefield due to a source located just below the ocean surface (black stars) for varying time. The bathymetric profiles of Figure 1 have been used: (a) North American west coast seafloor profile and (b) French coast seafloor profile. The same normalization coefficient has been used for all snapshots. The fundamental mode, the Airy phase of the first overtone and the fast seismic phase of the first overtone are emphasized by blue ellipses at $t = 150$ s. At $t = 300$ s, we observe the reflected and transmitted energy (blue ellipses). The source central time is set to 40 s.

Rayleigh waves are the main content in terms of amplitude of the vertical component oceanic and continental records. Instead, the relative amount of Rayleigh and Love waves on the horizontal components is still under debate and may vary in relation with the geographical region [e.g., Nishida *et al.*, 2008; Tanimoto *et al.*, 2015]. Since we perform 2-D numerical simulations, Love wave generation and coupling between Rayleigh and Love waves are prevented. Therefore, in this paper we only deal with vertical component records.

P waves are characterized by smaller amplitudes and they travel at 5.8 km/s below the seafloor. A zoom for the first 300 s of the oceanic station number 1 is shown above the seismograms in Figures 3a and 3b.

In order to investigate the seismic wavefield in terms of Rayleigh waves, we use the concept of local modes [Dahlen and Tromp, 1998, p.766] and we compute their basic properties in a vertically heterogeneous medium bounded by a free surface [Aki and Richards, 2009, p. 249]. In Appendix A we compute dispersion curves, synthetic seismograms and synthetic spectra of Rayleigh wave normal modes in a simple 1-D two-layer model, composed of ocean and crust [Herrmann, 2013]. Periods between 3 and 10 s and ocean depths of 5 km and 2 km are considered. Periods smaller than 3 s are shown in Figure A1 for the sake of completeness, but they are not considered in this study. A single source at the ocean surface has been used (source characteristics are detailed in section 2).

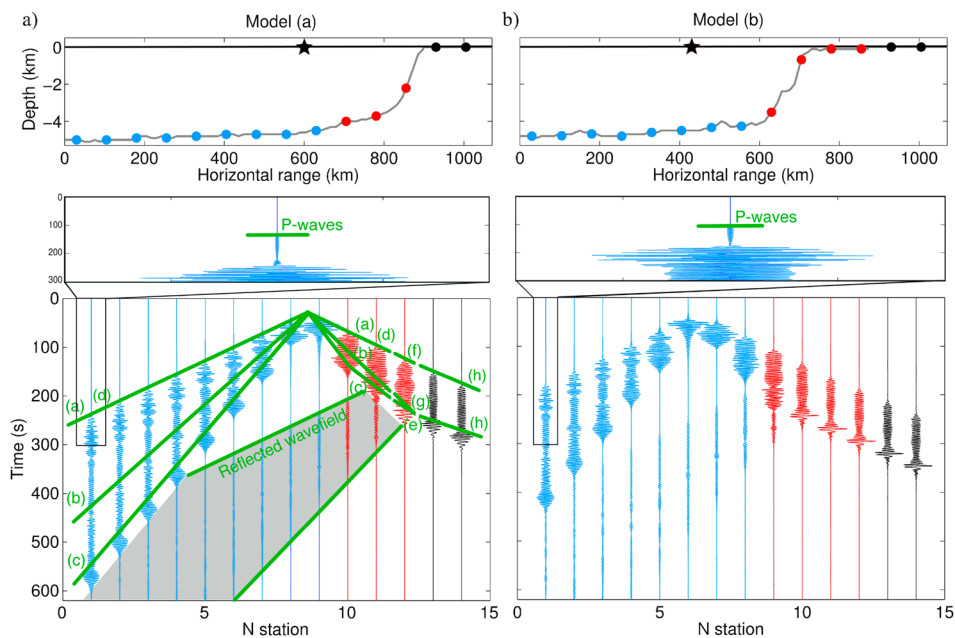


Figure 3. Vertical component of ground velocity synthetic seismograms filtered between 0.1 and 0.3 Hz and recorded just below the seafloor (blue), below the ocean-continent boundary (red) and on land (black). (a) North American west coast (model a in Figure 1); (b) French coast (model b in Figure 1). In both cases, the source (black star) is located 280 km away from the shelf break. A zoom on the P wave arrival is shown for the first oceanic traces ($t \leq 300$ s). We identify different seismic phases associated with the fundamental mode and the first overtone of Rayleigh waves: phase a: first overtone at low frequency in deep water, phase b: fundamental mode in deep water, phase c: Airy phase of the first overtone in deep water, phase d: second overtone in deep water, phase e: first overtone in shallow water, phase f: fundamental mode at low frequency in shallow water, and phase g: Airy phase of the fundamental mode in shallow water. Phase h denotes the continental fundamental mode. At the transition from deep to shallow water, the first overtone is converted to the fundamental mode. A small fraction of spread seismic energy is reflected back from the ocean-continent boundary (gray shadow). The source central time is set to 40 s. The same normalization coefficient has been used for all traces.

Figure A1 presents the group velocity (A1a and A1b, top) and the phase velocity (A1a and A1b, bottom) of Rayleigh wave normal modes. At these periods, i.e., between 3 and 10 s, the fundamental mode, the first and the second overtones show the presence of a minimum group velocity, called Airy phase [Pekeris, 1948], which has been observed in oceanic environments by, e.g., Press and Ewing [1948], Press et al. [1950], Ewing et al. [1957], Oliver and Ewing [1958], Ritzwoller and Levshin [2002], Harmon et al. [2012], and Tian and Ritzwoller [2015]. The Airy phase occurs at some given frequency which depends on the ocean thickness.

In deep water (Figure A1a, top), both the first and the second overtone show a minimum group velocity around a period of $T=3.6$ s. The first overtone Airy phase travels at about 1 km/s, whereas the second overtone Airy phase at about 2.1 km/s. The Airy phase of the fundamental mode in deep water occurs at longer periods, around $T=12$ s. The second overtone in deep water is characterized by a cutoff period of $T=3.8$ s. Higher overtones have a cutoff period smaller than the minimum period of interest in this study ($T=3$ s, red vertical line in Figure A1).

Instead, in relatively shallow water (Figure A1b, top), both the fundamental mode and the first overtone of Rayleigh waves are characterized by a minimum group velocity around 4 s. We observe that in shallow water, the first overtone is characterized by a cutoff period of about 4.1 s (Figure A1b, bottom). The second overtone in shallow water has a cutoff period smaller than the minimum period of interest in this study ($T=3$ s, red vertical line in Figure A1).

In Figure 3a, different seismic phases can be retrieved by comparing their local velocity with the group velocity dispersion curves shown in Figure A1. The same notation (green letters) has been used on both figures. Seismic waves recorded in deep water, i.e., seismograms recorded between station numbers 1 and 11 in Figure 3, travel with local group velocities shown in Figure A1a (top). Seismic waves recorded at station 12, located beneath 2 km of water, travel with group velocities shown in Figure A1b (top). Stations located on land, i.e., station

numbers 13 and 14, record continental Rayleigh waves, whose group velocity is about $0.9 \beta_c$, where β_c is the S wave velocity in the crust.

The first overtone of Rayleigh waves in deep water is strongly dispersive, as shown in Figure A1a. However, it is characterized by a broad maximum group velocity plateau at long periods—denoted as phase a, traveling at about 2.8 km/s—and a minimum group velocity around a period of $T = 3.6$ s, i.e., the Airy phase, at short periods—denoted as phase c, traveling at about 1 km/s. They mark the first and the last arrival on deep water records (i.e., at station from 1 to 11), respectively. The largest amplitude observed in deep ocean synthetic seismograms nearly corresponds to the minimum group velocity of the first overtone in Figure A1a (top), as shown in Figure A2a for both synthetic seismograms and spectra. Considering periods between 3 and 10 s, the second overtone of Rayleigh waves—seismic phase denoted as phase d—arrives slightly later with respect to the first overtone having maximum group velocity (phase a). The fundamental mode of Rayleigh waves in deep water—seismic phase denoted as phase b—travels with group velocities spanning from about 1.5 km/s to 1.1 km/s, at short and long periods, respectively. The amplitude of the fundamental mode is negligible with respect to the amplitude of the first overtone (blue versus red in Figure A2a).

Moving along the slope and approaching relatively shallow water, the long-period component of the first overtone (phase a) is progressively converted to the fundamental mode (phase f) (see Figure A1b, top).

At the ocean-continent boundary, the oceanic fundamental mode—denoted as phase g at short period and phase f at long period—is transmitted to the continent as fundamental mode (phase h). Moreover, the oceanic first overtone—denoted (phase e)—is converted to the continental fundamental mode (phase h). At continental stations, only the nondispersive fundamental mode of Rayleigh waves is recorded, traveling at about $0.9 \beta_c \approx 3$ km/s.

The fundamental mode and the first overtone of Rayleigh waves can be also observed in terms of instantaneous energy (Figure 2). For example, in Figure 2a, at $t = 150$ s, we observe the fundamental mode of Rayleigh waves around $x = 450$ km and the first overtone around $x = 350$ km (fast phase of the first overtone) and $x = 500$ km (Airy phase of the first overtone).

The small fraction of spread seismic energy reflected back from the ocean-continent boundary is visible in Figure 3 (emphasized by a gray shadow).

The waveform of land-recorded seismograms in model a and model b is nearly the same. Their amplitude is comparable, with a slightly larger amplitude on model b. The waveform energy—defined as the integral over time of the squared vertical velocity—is nearly the same in both cases (ratio equal to about 1).

In Figure 4, we show the power spectral density (PSD, $(\text{m/s})^2/\text{Hz}$) referencing synthetic seismograms in Figure 3. In each small black box we show the power spectral density in log scale (dB). Figure 4a is associated with model a and Figure 4b with model b, as shown in Figure 1. The same color notation of Figure 3 has been used: blue, red, and black spectra refer to traces recorded below the seafloor, along the ocean-continent boundary and on land, respectively.

All spectra are characterized by several local minima and maxima for varying frequency, which correspond to constructive and destructive interferences of local modes. This is a typical feature of spectra related to underwater measurements [e.g., Jensen *et al.*, 2011]. We observe that the spectral amplitude at short periods ($T < 6$ s) is larger than at long periods ($T > 6$ s) for all stations. An average difference of about 20 dB exists between the spectra at 3 and 10 s (black boxes in Figure 4). At long period ($T > 6$ s), the PSD of continental stations is larger than the PSD of oceanic stations, whereas the opposite occurs at short periods ($T < 6$ s). Continental PSD (black) shows a comparable amplitude between model a and model b.

4. The Ocean Site Effect

The ocean site effect influences the amplitude and the frequency content of land-recorded waveforms. In order to establish the role played by the ocean depth under the source—i.e., the ocean site effect—on the seismic wavefield, we compare synthetic seismograms due to a source close to the coast (in shallow water environment) with those due to a source offshore (in a deep water environment). Moreover, we filter the seismograms in two period bands: at short period, between 3 s and 6 s, and at long period, between 6 s and 10 s. The same bathymetric profile—model b in Figure 1—has been used with both sources.

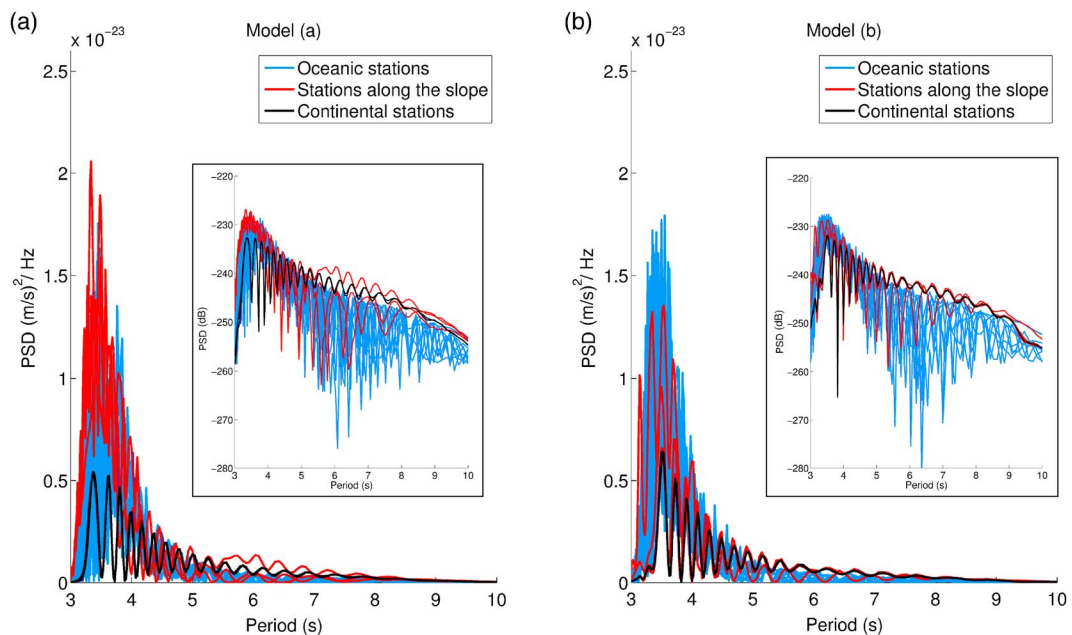


Figure 4. PSD ($(\text{m/s})^2/\text{Hz}$) of synthetic seismograms shown in Figure 3. (a) North American west coast (model a in Figure 1) and (b) French coast (model b in Figure 1). In each black box, the power spectral density is plotted in log scale (dB). The same color notation as in Figure 3 has been adopted: blue, red, and black spectra refer to traces recorded below the seafloor, along the ocean-continent boundary and on land, respectively. We observe that on both models, at short periods ($T \leq 5$ s), the PSD has larger amplitude at oceanic stations and along the ocean-continent slope. Instead, at long periods ($T \geq 5$ s), the PSD has larger amplitude on land and along the ocean-continent slope. The PSD recorded on the continent shows similar amplitude on both models.

Figure 5 shows the vertical component of ground velocity synthetic seismograms recorded below the seafloor (blue traces), below the ocean-continent boundary (red traces), and on land (black traces). Seismograms in Figure 5a refer to a source located at $x = 680$ km along the horizontal range, 30 km away from the continental shelf. Seismograms in Figure 5b are instead related to a source located 510 km away with respect to the continental shelf, at $x = 200$ km along the horizontal range, in a deep water environment. Sources are denoted as black stars on the two panels above the seismograms. The ocean depth below the source is about 2 km and 5 km, respectively. Green letters refer to seismic phases in Figure A1.

Land-recorded seismograms are affected by the ocean depth below the source. Considering periods between 3 s and 6 s—the seismograms in Figures 5a and 5b (middle)—a factor of 0.18 exists between the land-recorded energy—defined as the integral over time of the squared vertical velocity—in case of a source offshore (Figure 5b, middle) with respect to a source close to the shelf (Figure 5a, middle). Instead, considering periods between 6 and 10 s—the seismograms in Figures 5a and 5b (bottom)—a factor 1.48 exists between the land-recorded energy due to a source offshore (Figure 5b, bottom) and a source close to the continental shelf (Figure 5a, bottom). This difference in terms of energy suggests that at long period ($T > 6$ s), a source in deep water contributes more than a source in shallow water to land-recorded seismograms, whereas, on the contrary, at short period ($T < 6$ s), a source in shallow water contributes more than a source in deep water to land-recorded seismograms.

The PSD of synthetic seismograms in Figure 5 is shown in Figure 6. Figure 6a refers to the source located at $x = 680$ km and Figure 6b to the source located at $x = 200$ km along the horizontal range. Figure 6c shows the ratio between the land-recorded PSD due to the source in shallow and in deep water (the green line denotes a ratio equal to 1). The same color notation of Figure 5 has been used: blue, red, and black spectra refer to traces recorded below the seafloor, along the ocean-continent boundary and on land, respectively.

Comparing Figures 6a and 6b at short periods ($T < 6$ s), we observe that the relatively shallow water below the source in Figure 6a produces a larger amplification on both oceanic (blue) and continental (black) spectra than the deep water source in Figure 6b. Spectra referencing synthetic seismograms recorded along the slope (red)

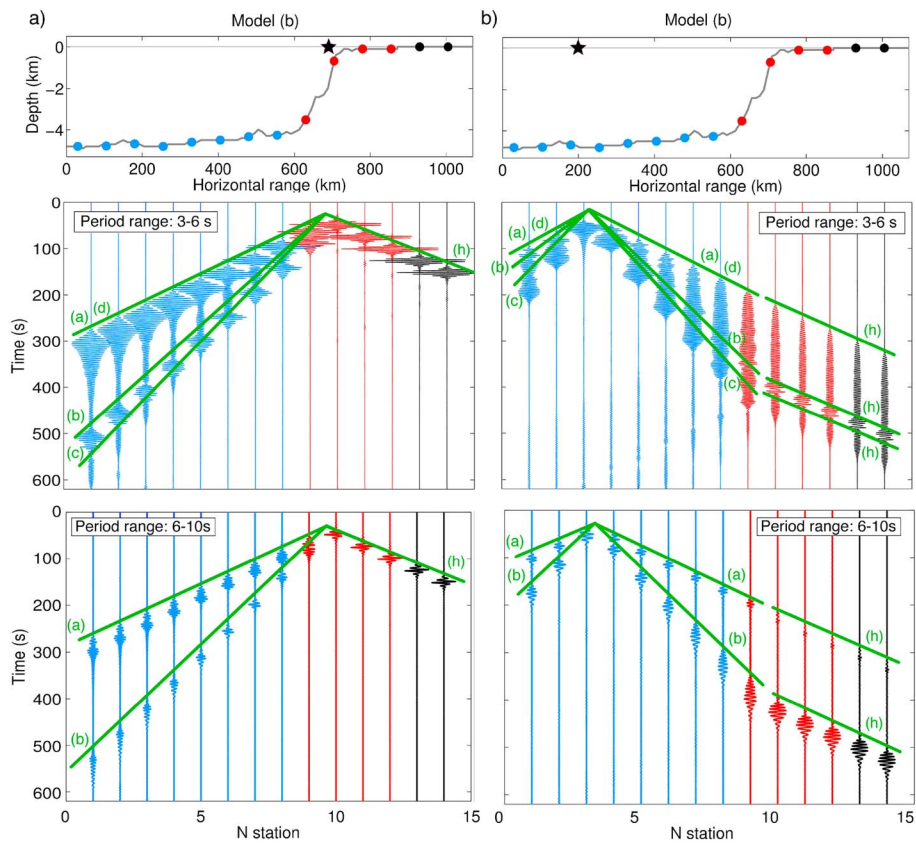


Figure 5. Vertical component of ground velocity synthetic seismograms filtered between 0.1 and 0.3 Hz and recorded below the seafloor (blue traces), below the ocean-continent boundary (red), and on land (black) for varying source location and period. (a) The source is located in shallow water, at $x = 680$ km. (b) The source is located in deep water, at $x = 200$ km. The French coast bathymetry (model b in Figure 1) has been used in both cases. Seismograms have been filtered between 3 s and 6 s (top seismograms) and between 6 s to 10 s (bottom seismograms). Green letters refer to seismic phases described in Figures 3 and A1. At short periods, the ratio between land-recorded total energy due a source in deep water and a source in shallow water is equal to 0.18, whereas at long periods it is equal to 1.48. Therefore, a source in deep water potentially contributes more to land-recorded long-period signals, whereas a source in shallow water to land-recorded short-period signals. In Figure 5b, we observe that the transmission to the continent occurs differently for the first overtone—fast phase (phase a) and Airy phase (phase c)—and the fundamental mode (phase b) of Rayleigh waves. The source central time is set to 40 s. For the sake of readability, traces filtered at long periods (Figures 5a and 5b, bottom) have been magnified by a factor of 3 with respect to traces filtered at short periods (Figures 5a and 5b, middle).

show instead a comparable amplitude. At long periods ($T > 6$ s), the deep water below the source produces a larger PSD at all stations than the relatively shallow water below the source.

In Figure 6c, we notice that the land-recorded power spectral density varies with both source location and period. A source in shallow water generates larger signals at short periods ($T < 6$ s) than a source in deep water. On the contrary, at long periods ($T > 6$ s) a source in deep water generates larger signals than a source in shallow water. As a consequence, land-recorded long-period signals are mostly due to deep water sources, whereas land-recorded short-period signals to sources in relatively shallow water, located close to the shelf.

5. The Seafloor Sediment Effect

As shown by *Gaultieri et al.* [2013] by comparing the site effect computed on a two-layer model and on the PREM (Preliminary Reference Earth Model) [Dziewonski and Anderson, 1981], the site effect on surface waves is not only due to the ocean depth but also due to the local structure below the source. It is a matter of fact that below the seafloor, a layer of sediments lies between ocean and crust. *Ardhuin et al.* [2013] and *Gaultieri* [2014] show, by using two different methods, that a sedimentary layer may strongly affect this site effect.

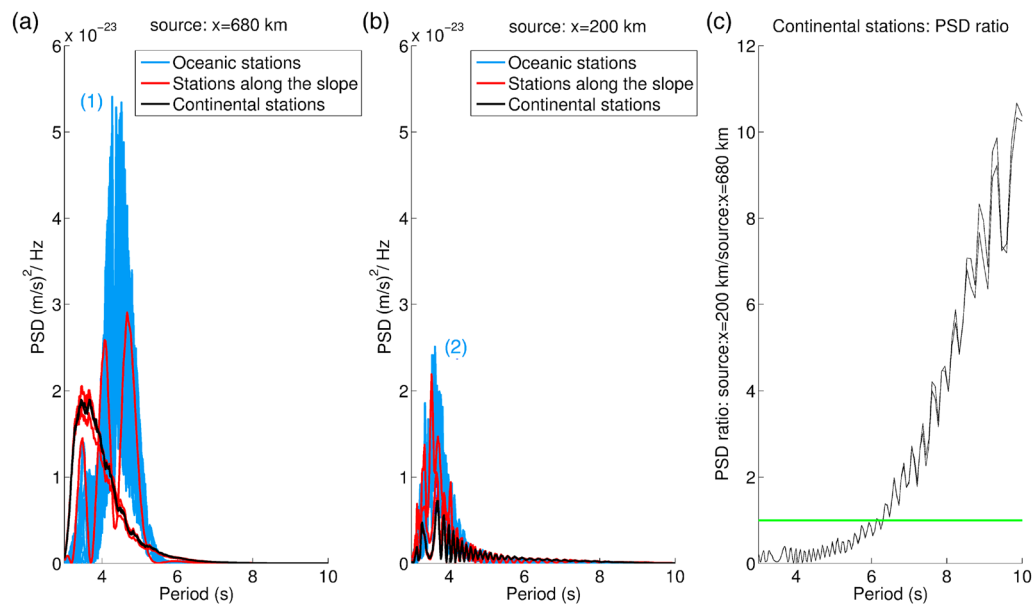


Figure 6. PSD ($(\text{m/s})^2/\text{Hz}$) of synthetic seismograms shown in Figure 5 for a source located above (a) shallow water, at $x = 680 \text{ km}$, and (b) deep water, at $x = 200 \text{ km}$. (c) The ratio between the land-recorded PSD due to a source in deep and shallow water. The same color notation as in Figure 5 has been adopted: blue, red, and black spectra correspond to traces recorded below the seafloor, along the ocean-continent boundary and on land, respectively. Both oceanic (blue) and continental (black) PSDs due to a source in shallow water (Figure 6a) are more amplified than the PSDs due to a source in deep water (Figure 6b). Spectra recorded along the slope (red) show a comparable amplitude. The maximum peak of oceanic PSDs due to a shallow (Figure 6a) and a deep (Figure 6b) water source occurs at different periods, and it is due to different seismic phases. The PSD peak (1) is due to the Airy phase of the fundamental mode in shallow water, whereas the PSD peak (2) is due to the Airy phase of the first overtone in deep water (see Appendix A for more details). (c) The land-recorded PSD due to a source in shallow water is smaller (larger) at periods $T > 6 \text{ s}$ ($T < 6 \text{ s}$) than the land-recorded PSD due to a source in deep water. The green line in Figure 6c refers to a ratio equal to 1.

Worldwide, the seafloor sediment coverage spans from few meters up to thousand of meters. Along the seafloor profile in model a (Figure 1), the sedimentary layer is quite uniform and reaches a maximum depth of 500 m. Along the seafloor profile in model b instead the sedimentary layer spans from few hundreds meters to a $\sim 7 \text{ km}$ thick sedimentary basin, lying about 250 km away from the coastline.

In this section, the role played by this sedimentary basin on oceanic and land-recorded seismograms is investigated. Three source locations are considered: (a) between the sedimentary basin and the continental shelf, (b) above the sedimentary basin, and (c) beyond the sedimentary basin, far away with respect to the coast. The ocean depth below the three sources is nearly the same. As a consequence, the amplification effect due to the ocean depth is nearly the same in all the three cases, and we are able to focus on the effect due to the sedimentary layer.

A simple explanation in terms of local modes is not possible in this case since the layer of sediments enhances leakage phenomena. Moreover, interface waves—called Scholte waves in case of a liquid-solid interface [Scholte, 1947]—may be generated also at these periods. Therefore, in this section, we only focus on the analysis of the effects due to the layer of sediments on the amplitude of seismic traces recorded at the ocean bottom and on land.

In Figure 7, instantaneous energy generated by these three sources are shown for varying time. The seafloor and the sediment-crust interfaces are drawn with black lines. The source is located at $x = 600 \text{ km}$ in Figure 7a, at $x = 430 \text{ km}$ in Figure 7b, and at $x = 200 \text{ km}$ in Figure 7c. The same normalization coefficient is used for all snapshots.

Both the ocean and the sedimentary layer act as a waveguide, significantly reducing the amount of energy which passes through the sediment-crust interface. Acoustic P waves and elastic P and S waves are multiply reflected within the ocean and the sedimentary basin, respectively. Most of the energy is trapped by the sedimentary layer.

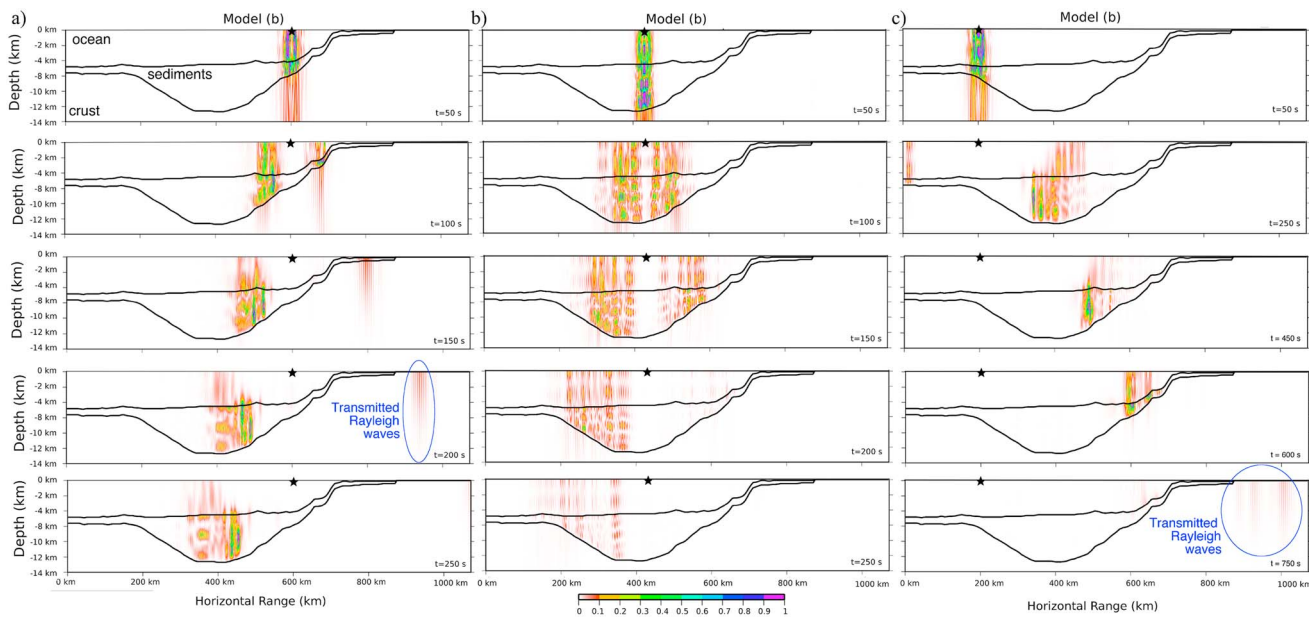


Figure 7. Instantaneous energy for varying time associated with the seismic wavefield due to a source located: (a) between the sedimentary basin and the continental shelf, (b) above the sedimentary basin, and (c) beyond the sedimentary basin, far away with respect to the coast. The same seafloor profile has been used in all cases (model b in Figure 1). The ocean depth below the three sources is nearly the same, whereas the sedimentary thickness strongly varies. Most of the energy is trapped by the sedimentary layer in all cases, but the amount of land-transmitted energy depends on the thickness of sediments below the source. Land-transmitted energy is characterized by the same order of magnitude in Figures 7a and 7c (blue ellipses), whereas is negligible in Figure 7b. The source central time is set to 40 s.

The amount of land-transmitted energy depends on the sediment thickness below the source. In Figures 7a and 7c, the source is located ahead and beyond the sedimentary basin with respect to the coast, respectively. The thickness of the sedimentary layer below the source is nearly the same in both cases. A fraction of instantaneous energy is transmitted on land after 200 s if the source is located close to the coast (Figure 7a) and after 750 s if the source is offshore (Figure 7c). Although the land-transmitted energy is characterized by the same order of magnitude, it is slightly larger if the source is close to the coast (Figure 7a at $t = 200$ s) than if the source is offshore (Figure 7c at $t = 750$ s).

In Figure 7b, the source is located just above the sedimentary basin. In this area, the thickness of sediments reaches about 7 km. We observe that the energy is strongly trapped by the sedimentary basin and the amount of land-recorded energy is negligible with respect to that observed in Figures 7a and 7c.

In order to quantify and compare the energy amount recorded below the seafloor and transmitted on land in these three cases, ground velocity synthetic seismograms have been computed. Figure 8 shows the vertical component of seismograms recorded below the seafloor, i.e., inside the sedimentary basin (blue traces), below the ocean-continent boundary (red traces) and on land (black traces). The source location is shown on the panels above the seismograms (black star) and corresponds to the three cases in Figure 7. All traces have been normalized by the same factor as in Figures 3 and 5.

As already observed for the instantaneous energy in Figure 7, if the source is located above a thick layer of sediments (Figure 8b), land-recorded signals are negligible with respect to the case in which the source is located above a thin sedimentary layer (Figures 8a and 8c). The land-recorded energy—defined as the integral over time of the squared vertical velocity—in Figure 8a is 53.3 times larger than the one in Figure 8b. Short-period signals mostly contribute to this difference: these ratios are around 60 when filtering the seismograms between $T = 3$ s and $T = 6$ s and around 20 when filtering the seismograms between $T = 6$ s and $T = 10$ s.

Land-recorded seismograms due to a source ahead (Figure 8a) and beyond (Figure 8c) the sedimentary basin are comparable. Indeed, the energy ratio between signals due the source ahead and beyond the sedimentary basin is 1.06.

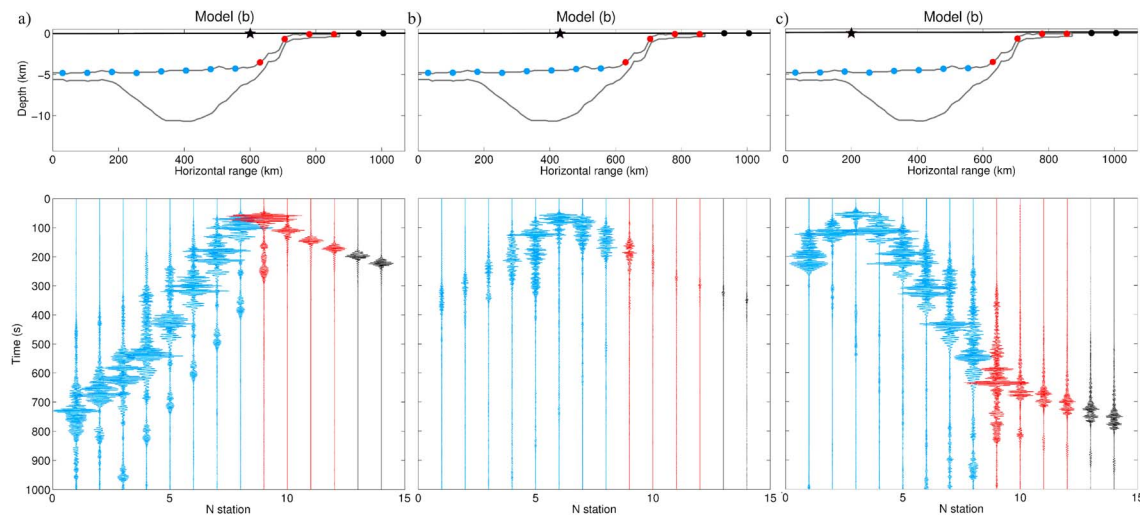


Figure 8. Vertical component of ground velocity synthetic seismograms filtered between 0.1 and 0.3 Hz and recorded below the seafloor (blue traces), below the ocean-continent boundary (red traces), and on land (black traces) in the presence of seafloor sediments for varying source locations (black stars). The source is located: (a) between the sedimentary basin and the continental shelf, (b) above the sedimentary basin, and (c) beyond the sedimentary basin, far away with respect to the coast. The same seafloor profile has been used in all cases (model b in Figure 1). If the source is located above a thick layer of sediments (Figure 8b), land-recorded signals are negligible with respect to the cases in which the source is located above a thin layer of sediments (Figures 8a and 8c). A factor 53.3 exists between the land-recorded energy in Figures 8a and 8b and a factor 51.5 between the land-recorded energy in Figure 8c and 8b. Instead, land-recorded maximum amplitudes due the source beyond (Figure 8c) and ahead the sedimentary basin (Figure 8a) are comparable, with only a factor 1.06 between them. The source central time is set to 40 s.

The sediment thickness below the source region, i.e., the source site effect due to seafloor sediments, is then the main control parameter of land-recorded signal amplitude. Compared to the case without sediments, we observe that if the sedimentary layer below the source region is thin (i.e., up to 1 km in our modeling), it does not significantly affect land-recorded seismograms. Land-recorded energy due to a source at $x = 200$ km in the absence of sediments (Figure 5b) is a factor 1.20 larger than the land-recorded energy in the presence of sediments (Figure 8c). This difference is emphasized at long periods ($T = 6\text{--}10$ s), where a factor 3.33 exists between them.

On the other hand, if the sedimentary layer below the source region is thick (i.e., up to 7 km in our modeling), the amplitude of land-recorded seismograms strongly decreases. Indeed, land-recorded energy due to a source at $x = 430$ km in the absence of sediments (Figure 3b) is a factor 100 larger than land-recorded energy in the presence of sediments (Figure 8b). This factor reaches its maximum at long periods ($T = 6\text{--}10$ s), where it is equal to 666.

In all cases in Figure 8, we observe that synthetic seismograms recorded below the seafloor—station number from 1 to 9—are much longer in time than the synthetic seismograms computed in the absence of sediments (Figures 3 and 5). This is due to the propagation within the sedimentary basin, which slows down seismic waves and enhances reverberation effects.

In Figure 9, we show the PSD of synthetic seismograms in Figure 8. Green, blue, and red spectra refer to oceanic station number 1–3, 4–8, and 9–12, respectively. Black spectra refer to continental traces. The sedimentary basin lies between station numbers 4 and 8 (blue spectra). We observe stronger excitation for periods shorter than about 6 s with respect to longer periods.

In Figures 9a and 9c, where the sedimentary layer below the source is thin, the PSD associated with oceanic stations—station numbers from 1 to 12, i.e., green, blue, and red spectra—have comparable amplitude. Moreover, land stations (black spectra) show a smaller PSD with respect to oceanic stations and a comparable amplitude between them.

In Figure 9b, where the sedimentary layer below the source is thick, the PSD shows a maximum for stations located inside the basin (station number from 4 to 8, i.e., blue spectra). The PSD associated with continental stations (black) is negligible with respect to oceanic stations.

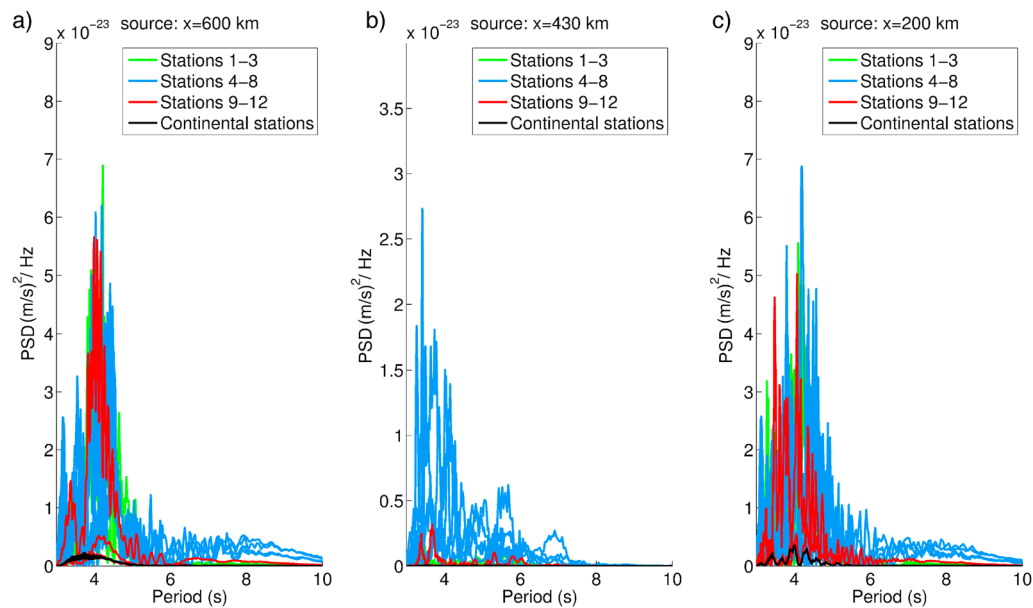


Figure 9. PSD ($(\text{m/s})^2/\text{Hz}$) of synthetic seismograms shown in Figure 8 for a source located (a) between the sedimentary basin and the continental shelf, (b) above the sedimentary basin, and (c) beyond the sedimentary basin, far away with respect to the coast. Green, blue, and red spectra refer to oceanic stations. Black spectra refer to continental traces. The sedimentary basin lies between station number 4 and 8 (blue spectra). In general, we observe that seismic waves filtered at periods $T < 6$ s are more excited than seismic waves at longer periods. In Figures 9a and 9c, where the sedimentary layer below the source is thin, the power spectral density associated with oceanic stations—station numbers from 1 to 12, i.e., green, blue, and red spectra—have comparable amplitude. Continental stations—station numbers 13 and 14—show a comparable PSD, smaller than oceanic stations. In Figure 9b, where the sedimentary layer below the source is thick, all the energy is trapped inside the sedimentary basin and it is mostly recorded by stations 4 to 8 (blue). The power spectral density associated with continental stations (black) is negligible with respect to oceanic stations.

A comparison between the power spectral density of land-recorded synthetic seismograms in the presence (red) and in the absence (black) of sediments is shown in Figure 10 for two source locations: (a) at $x = 200$ km, 520 km away with respect to the shelf break, and (b) at $x = 430$ km, 280 km away from the shelf break. Spectra in Figure 10a refer to synthetic seismograms in Figure 5b (black, absence of sediments) and Figure 8c (red, presence of sediments). Spectra in Figure 10b refer to synthetic seismograms shown in Figure 3b (black, absence of sediments) and Figure 8b (red, presence of sediments). We observe that if the sedimentary layer below the source is thin (Figure 10a), even if the source is located beyond the sedimentary basin, land-recorded power spectral density is affected only at long periods ($T > 6$ s). However, if the sedimentary layer below the source is thick (Figure 10b), the land-transmitted PSD is negligible with respect to the case without sediments at all periods.

6. Discussion

In the previous sections, three of the main factors which affect the seismic wavefield generated by a single source at the ocean surface have been analyzed: the ocean-continent boundary effect, the ocean site effect, and the effect due to the seafloor sediment layer. In the following, we summarize the main achieved results, and we compare them with field data from previous studies.

6.1. Main Numerical Results

The ocean-continent boundary effect. The effect of the ocean-continent boundary has been studied by comparing land-recorded signals in a two-layer model—ocean and crust—characterized by two different bathymetries.

1. At the transition from deep to shallow water, the first overtone is converted to the fundamental mode of Rayleigh waves. At the ocean-continent boundary, the oceanic fundamental mode is transmitted to the continent and the oceanic first overtone is converted to the continental fundamental mode.
2. If the source is in deep water, oceanic PSDs at short periods ($T < 6$ s) are always larger than continental PSDs.

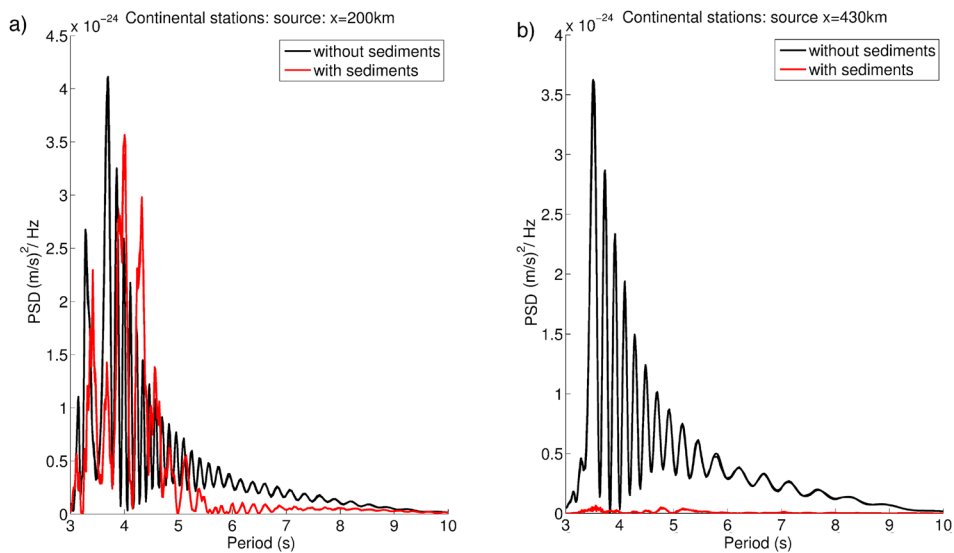


Figure 10. Comparison between the power spectral density of land-recorded synthetic seismograms in the presence (red) and in the absence (black) of sediments for two source locations: (a) at $x = 200$ km, 520 km away with respect to the shelf break and (b) at $x = 430$ km, 280 km away from the shelf break. Spectra in Figure 10a refer to synthetic seismograms shown in Figure 5b (black, absence of sediments) and Figure 8c (red, presence of sediments). Spectra in Figure 10b refer to synthetic seismograms shown in Figure 3b (black, absence of sediments) and Figure 8b (red, presence of sediments). We observe that in the presence of a thin sedimentary layer below the source, the PSD of continental stations is mostly affected at periods $T > 5$ s with respect to the case without sediments. Instead, in the presence of a thick sedimentary layer below the source, the PSD of continental stations is always lower than the PSD of continental stations obtained in a medium without sediments.

3. Considering two different bathymetries, the amplitude of the PSD recorded on the continent is fairly similar and the waveform energy is nearly the same.
4. Only a small fraction of seismic waves is reflected back from the ocean-continent boundary, toward the open ocean.

The ocean site effect. The ocean site effect has been studied by comparing the seismic wavefield generated by a source close to the coast, in a shallow water environment, and a source offshore, in a deep water environment.

1. If the source is in deep water, the amplitude of seismograms recorded in deep water is dominated by the first overtone of Rayleigh waves, which is characterized by a large amplitude Airy phase at periods around $T = 3.6$ s traveling at about 1 km/s.
2. PSDs at short periods ($T < 6$ s) are larger than PSDs at long periods ($T > 6$ s) for all stations.
3. Land records are strongly frequency dependent: a source in deep water potentially contributes more to land-recorded long-period signals ($T > 6$ s), whereas a source in shallow water contributes more to land-recorded short-period signals ($T < 6$ s).

The seafloor sediment effect. The effect due to the seafloor sediment layer has been studied by comparing the seismic wavefield generated by three sources having different locations with respect to a sedimentary basin.

1. The amount of land-transmitted energy depends on the sediment thickness below the source region. If the source is located above a thick layer of sediments, land-recorded signals, and PSDs are negligible with respect to the cases in which the source is located above a thin layer of sediments.
2. The PSD associated with continental stations is negligible with respect to oceanic stations in the case when the source is located above a thick layer of sediments.

6.2. Comparison With Field Data

In this section, we compare our predictions with previously published field data based on the cross correlation of seismic noise records and beamforming analysis.

Although our results cannot be directly linked to Green's function analysis via cross-correlation technique, which considers the source at the seafloor, many observed features are consistent and can be explained by our analysis.

Several studies have shown the presence of a slow seismic phase in vertical component records, traveling with a velocity of about 1 km/s [Press and Ewing, 1948; Press et al., 1950; Ewing et al., 1957; Oliver and Ewing, 1958; Ritzwoller and Levshin, 2002; Harmon et al., 2012; Tian and Ritzwoller, 2015]. This phase corresponds to the Airy phase of the fundamental mode of Rayleigh waves if the source is in shallow water and to the Airy phase of the first overtone if the source is in deep water, as shown in our synthetic simulations (e.g., Figures 3, 5 and Appendix A). Harmon et al. [2012] observe the Airy phase between 6 s and 9 s, with velocities ranging from 0.93 to 0.95 km/s, due to the presence of an ocean layer thicker than 3 km. This is consistent with our modeling. In fact, considering a model composed of ocean and crust, we expect to have the Airy phase of the fundamental mode of Rayleigh waves at $T \sim 6.5$ s for an ocean 3 km deep and at $T \sim 8.5$ s for an ocean 4 km deep.

Both the fundamental mode and the first overtone of Rayleigh waves have been found in interferometry ocean bottom data analysis. The fundamental mode of Rayleigh waves has been seen on the vertical component of noise records at all periods from 3 to 10 s [e.g., Harmon et al., 2007; Yao et al., 2011]. Instead, the first overtone of Rayleigh waves appears only at short periods (shorter than about $T = 7$ s in Harmon et al. [2007] and shorter than about $T = 4$ s in Yao et al. [2011]). Analysis performed only at longer periods have not shown the presence of the first overtone on the vertical component of noise records (see, e.g., Takeo et al. [2013] for periods larger than $T = 14$ s). This confirms the presence of a cutoff period for the first overtone of Rayleigh waves, which varies with the ocean depth within the studied region. For example, the theoretical cutoff period of the first overtone in the configuration of Harmon et al. [2007]—i.e., ocean depth equal to 3.5 km—is 7.4 s, considering the two-layer model composed of ocean and crust. This is consistent with their observation ($T \simeq 7$ s).

Bromirski et al. [2013] and Stephen et al. [2013] point out that land-recorded noise spectra are more affected by sources in shallow water at short period and by sources in deep water at long period. This is consistent with our results, which show that a source in deep water contributes more than a source in shallow water to land-recorded signals at long period ($T > 6$ s), whereas the opposite occurs at short period ($T < 6$ s).

7. Conclusion

In this paper, we investigate the seismic wavefield generated by a source located at the ocean surface, in the period band $T=3-10$ s, and three of the major factors which shape the seismic wavefield: the ocean-continent boundary, the source location with respect to the local ocean depth, and the thickness of seafloor sediments. The seismic wavefield generated by a pressure source located just below the ocean surface has been modeled using the 2-D spectral element method.

This work aims to clarify the fact that a deep water noise source can contribute to the noise level recorded on land, especially at long period ($T > 6$ s), in the secondary microseismic frequency band and that seafloor sediments below the source region play a major role on microseismic propagation. The presence or the absence of the continental shelf has instead a limited effect on land-recorded noise level.

More geographic regions and more features—such as seismic attenuation, bathymetric roughness, seafloor hills, and crust thickness variations—will be analyzed in the future. The extension of the spectral element method in 3-D may allow us to study the wavefield recorded on the horizontal components and the generation of seismic noise Love waves. This approach may also be extended to longer periods considering appropriate sources [Ardhuin et al., 2015] in order to study the wavefield of the seismic "hum."

Appendix A: The Source Site Effect: Deep Versus Shallow Water Source

In this appendix, we evaluate the effect of the ocean depth on Rayleigh waves considering a source in deep and in shallow water. A simple 1-D two-layer Earth model, composed of ocean and crust, is used. The same elastic properties detailed in section 2 are considered.

We use the concept of local modes [Dahlen and Tromp, 1998, p. 766] in order to investigate the seismic wavefield in terms of Rayleigh waves. It is well known that in a flat laterally homogeneous structure, surface waves can be described as a superposition of fundamental and higher modes, which propagate independently. Local modes are the surface-wave modes that would propagate in a fictitious laterally homogeneous model having properties of the laterally varying model at the considered location [Maupin, 1988]. Local modes can

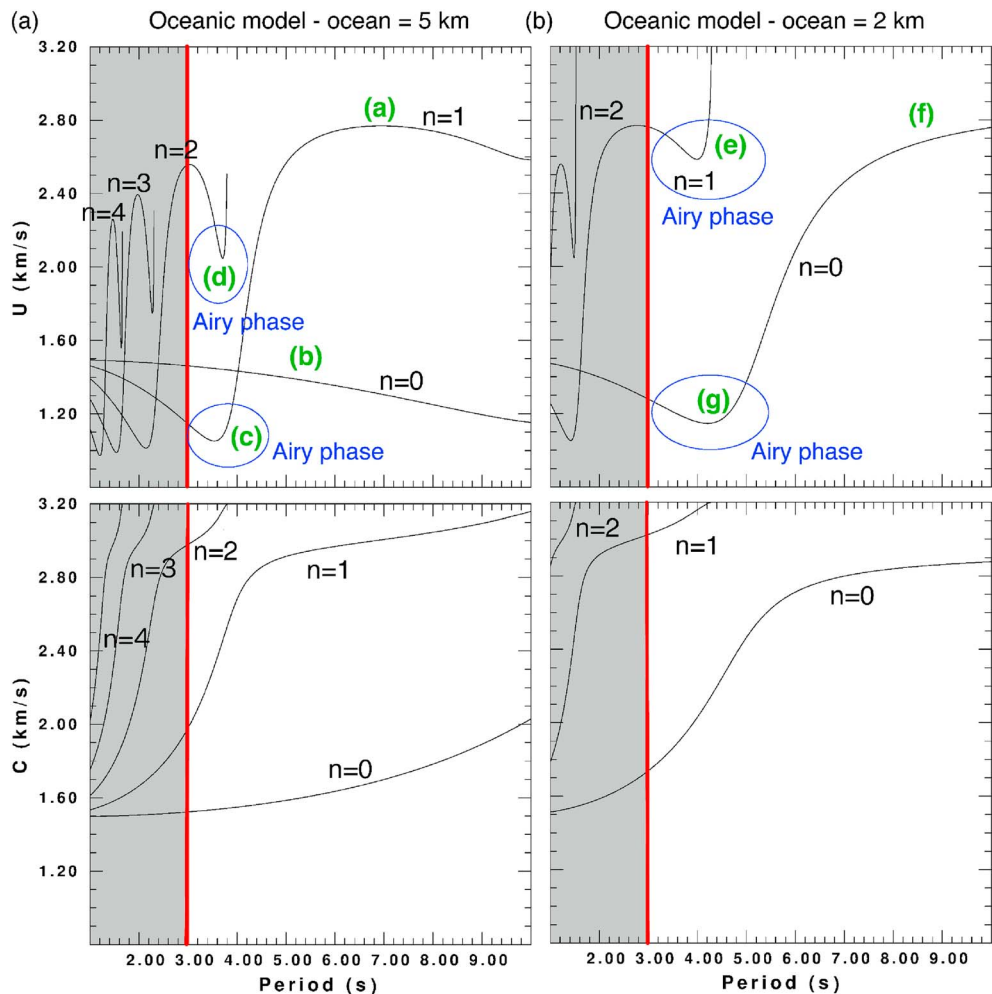


Figure A1. Group velocity of Rayleigh wave normal modes as a function of period computed in a flat two-layer model with an ocean of (a) 5 km and (b) 2 km (top). Phase velocity of Rayleigh wave normal modes as a function of period computed in a flat two-layer model with an ocean of (a) 5 km and (b) 2 km (bottom). The red line denotes the minimum period considered in this study. Green letters refer to the seismic phases observed in the synthetic seismograms shown in Figures 3 and 5. The Airy phase of the fundamental mode, the first and the second overtone is emphasized by blue ellipses. We denote the fundamental mode as $n=0$ and the overtones with increasing radial order n . The cutoff period of the first overtone ($n=1$) in shallow water is about 4.1 s, whereas the cutoff period of the second overtone ($n=2$) in deep water is 3.8 s. We notice that in the two-layer model, higher overtones have cutoff periods smaller than 3 s (gray area) and only two (three) modes exist in shallow (deep) ocean at longer periods, i.e. in the period range of interest.

be used in slowly laterally varying structures [Woodhouse, 1974]. Synthetic seismograms can be written as superposition of local modes, given by the product of the source site effect (through the value of the vertical eigenfunction at the source location), the receiver site effect (through the value of the eigenfunction at the receiver location for each component), and a term which accounts for the propagation (through traveltime, attenuation, and geometrical spreading).

Figure A1 presents the group velocity (A1a and A1b, top) and the phase velocity (A1a and A1b, bottom) of the fundamental mode, the first and the second overtone of Rayleigh waves, considering ocean depths of 5 and 2 km, respectively.

In Figure A2 are shown synthetic seismograms and spectra. The computation has been performed by wave number integration [Herrmann, 2013] for a station located 400 km away from the source, 1 m below the seafloor in both cases. We consider a pressure point source, located 1 m below the ocean surface. All seismograms have been filtered between 0.1 and 0.3 Hz, the secondary microseismic frequency band, as for the spectral element computations shown in this study. The ocean thickness is 5 km for seismograms shown in Figure A2a and 2 km for seismograms in Figure A2b. Seismograms shown on both figures have been

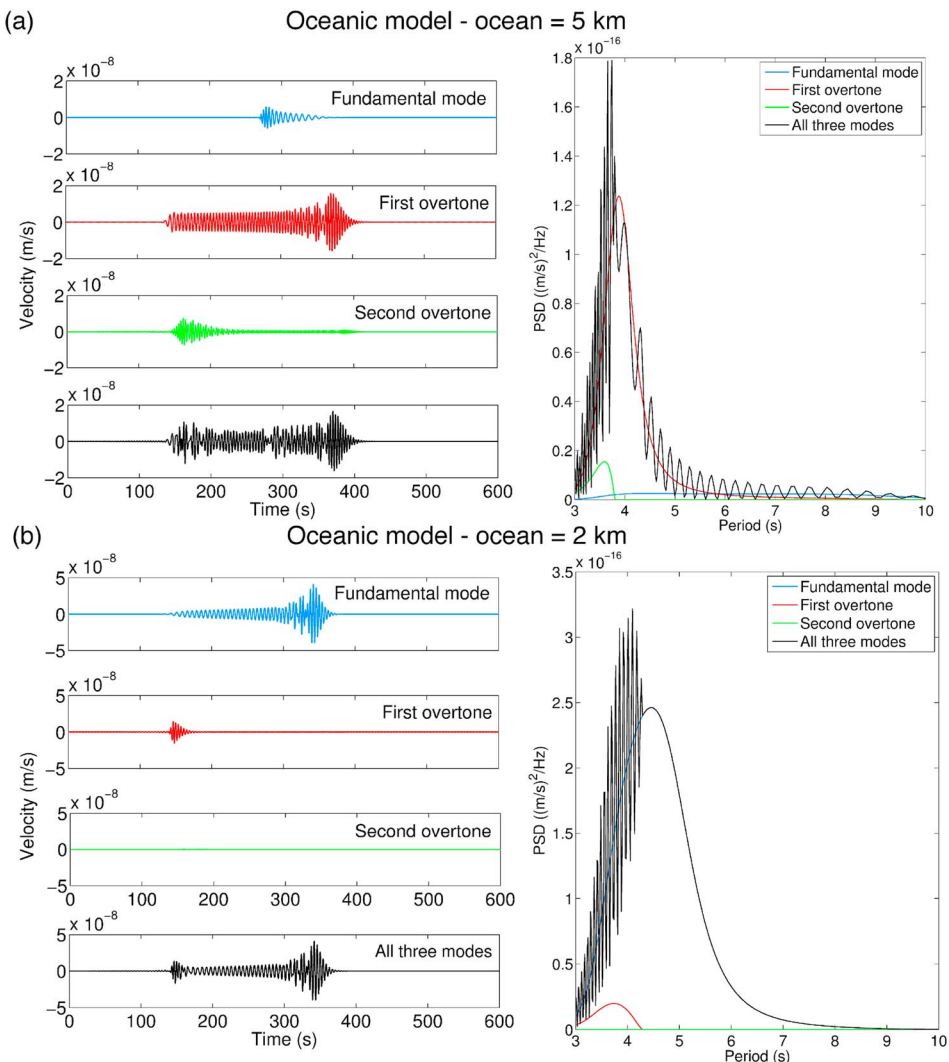


Figure A2. Synthetic seismograms and spectra computed in a flat two-layer Earth model, composed of ocean and crust. The ocean thickness is (a) 5 km and (b) 2 km. A pressure point source is located 1 m below the ocean surface and a receiver is set 1 m below the seafloor in both cases. The horizontal distance between the source and the station is 400 km. The computation has been performed considering the fundamental mode only (blue), the first overtone only (red), the second overtone only (green), and all the three modes together (black). We observe that in deep water (Figure A2a), the amplitude of the first overtone is larger than the amplitude of the fundamental mode, whereas in relatively shallow water (Figure A2b) the fundamental mode dominates in terms of amplitude with respect to the first overtone. In deep water (Figure A2a) the maximum PSD is due to the Airy phase of the first overtone, whereas in shallow water (Figure A2b) the maximum PSD is due to the Airy phase of the fundamental mode of Rayleigh waves. The second overtone contributes only in deep water and for periods smaller than 3.8 s. The cutoff period of the first overtone in shallow water is about 4.1 s, whereas the cutoff period of the second overtone in deep water is 3.8 s, as shown in Figure A1.

computed considering only the fundamental mode (blue), only the first overtone (red), only the second overtone (green), and all the three together (black).

Seismograms in Figure A2a are computed in a two-layer model with an ocean thickness of 5 km, typical of ocean basins. The fundamental mode of Rayleigh waves (blue seismogram) travels with a group velocity around 1.5 km/s, compatible with the group velocity dispersion curve in Figure A1a (seismic phase denoted as phase b in Figure A1a). Adding the first overtone (red seismogram), we notice that the fundamental mode is one order of magnitude smaller than the first overtone. The first overtone shows a quite strong dispersion behavior (Figure A1a), with group velocities from about 1 km/s to 2.8 km/s. As shown in Figure A1, the slowest phase corresponds to a minimum group velocity (seismic phase denoted as phase c in Figure A1a),

which is the largest signal in terms of amplitude (Figure A2a, red seismogram). This phase has been called Airy phase in the literature [Pekeris, 1948], and it has been observed on oceanic records by, e.g., Press and Ewing [1948] Press et al. [1950], Ewing et al. [1957], Oliver and Ewing [1958], and Ritzwoller and Levshin [2002]. The second overtone (green seismogram) contributes only at periods shorter than 3.8 s—its cutoff period in deep water, as shown in Figure A1a (top). Along the black spectrum, we notice a larger number of minima and maxima at periods smaller than 3.8 s with respect to longer periods. This is due to the constructive and destructive interferences of the three modes at short periods.

Seismograms in Figure A2b are computed in a two-layer model with an ocean thickness of 2 km, typical of ocean-continent boundary regions. The fundamental mode of Rayleigh waves (blue seismogram) shows a strong dispersion behavior, as already observed in Figure A1b (top). The slowest phase corresponds to the Airy phase (seismic phase denoted as phase g in Figure A1b (top)), the minimum of the dispersion curve of the fundamental mode, which occurs around 4 s (Figure A1b, top). Adding the first overtone (red seismogram), a fast signal arrives before the fundamental mode, with a group velocity spanning from 2.6 to 3.2 km/s (seismic phase denoted as phase e in Figure A1b (top)). Its amplitude is comparable with the amplitude of the Airy phase of the fundamental mode of Rayleigh waves. We observe that the first overtone is characterized by a cutoff period of about 4.1 s (Figure A1b, bottom). The second overtone (green seismogram) gives no contribution in shallow water at these periods.

From Figures A1a and A1b (bottom), we also observe that in the period band 3–10 s and in the two-layer model, there are no Scholte waves. In fact, the phase velocity of all modes is always larger than the P wave velocity in the ocean, i.e., $\alpha_w > 1.5$ km/s [e.g., Biot, 1952]. Therefore, in this system, only Rayleigh waves are observed. A similar observation has been done by Gualtieri et al. [2013] in case of the PREM model. On the contrary, in the presence of seafloor sediments, Scholte waves may be present at these periods. Therefore, in the presence of sediments, we should more properly talk about Scholte-Rayleigh waves.

Appendix B: Noise Sources: Where They Are and Why it Matters

Seismic noise is generated by the superposition of ocean waves coming from nearly opposite directions in extended oceanic regions, associated with storms. Extended sources can be schematized by a grid of point sources [Longuet-Higgins, 1950; Gualtieri et al., 2013]. Seismic waves coming from different point sources interfere and generate the seismic noise wavefield that we record at seismic stations. In order to understand the seismic noise content in terms of seismic waves and to avoid interferences from different sources, one single source has been employed in this study.

Seismic noise at a given frequency is generated by the interaction of half-frequency ocean gravity waves driven by wind and whose restoring force is gravity, coming from nearly opposite directions [Longuet-Higgins, 1950; Hasselmann, 1963]. Gravity dominantly controls the pressure field in a close-to-surface layer, whose thickness is comparable with the wavelength of ocean gravity waves [Longuet-Higgins, 1950]. Compressibility (seismic P waves) plays instead the dominant role on the pressure field in the remaining part of the ocean. With the exception of coastal regions and at periods associated with the generation of secondary microseisms, the wavelengths of ocean gravity waves are typically smaller than ocean depths. Because of that, noise sources are located at the ocean surface, or just below it, and they generate acoustic waves, i.e., P waves, which travel within the ocean.

From the ocean surface, acoustic P waves reach the seafloor where they are partially transmitted to the solid ground both as P and S waves and partially reflected in the water layer as P waves. In the ocean, P waves are multiply reflected between the seafloor and the ocean free surface and they produce a site effect on the seismic wavefield below the seafloor which varies with frequency and ocean depth [e.g., Longuet-Higgins, 1950; Gualtieri et al., 2013; Arduin and Herbers, 2013; Gualtieri et al., 2014].

The site effect depends on the source location and it acts differently on body and surface waves [Gualtieri et al., 2014]. For Rayleigh wave normal modes, the source site effect is related to the value of the eigenfunction at the source depth [Gualtieri et al., 2013; Tanimoto, 2013]. Therefore, if the source is located below the seafloor, in the solid ground, as in Ying et al. [2014], the source site effect acts differently with respect to the case of the source located at the ocean surface. As a consequence, surface waves generated below the seafloor may have different amplitudes between these two cases.

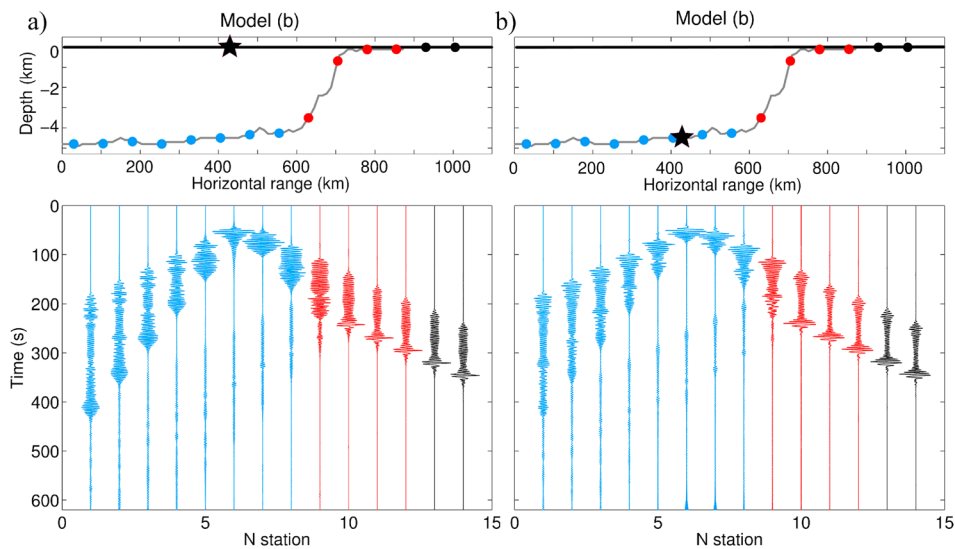


Figure B1. Vertical component of ground velocity synthetic seismograms filtered between 0.1 and 0.3 Hz and recorded below the seafloor (blue traces), below the ocean-continent boundary (red traces) and on land (black traces) due to a source (black star) located: (a) just below the ocean surface and (b) just below the seafloor. The same seafloor profile has been used in both cases (model b in Figure 1). We note the presence of the Airy phase of the first overtone in deep water, traveling at about 1 km/s, which is more amplified if the source is in the water layer. The source central time is set to 40 s. The same normalization coefficient has been used for all traces.

In Figure B1, we compare the vertical component of synthetic seismograms due to a source at the ocean surface (Figure B1a) and a source below the seafloor (Figure B1b). These seismic traces are recorded below the seafloor (blue traces), below the ocean-continent slope (red traces) and on land (black traces). Since we are not interested in absolute amplitudes, all seismograms have been normalized. Since the sources are located in two different media, characterized by different elastic parameters—the ocean layer in Figure B1a and the crust in Figure B1b—in order to get equivalent source amplitudes, a scale factor has to be applied [e.g., Capdeville and Marigo, 2007, their Appendix A]. As a consequence, two different normalization constants are required, one for Figure B1a and one for Figure B1b. The two normalization constants have been chosen equal to 10^{-11} m/s for Figure B1a and 10^{-15} m/s for Figure B1b in order to get 1 for the maximum amplitude in both cases.

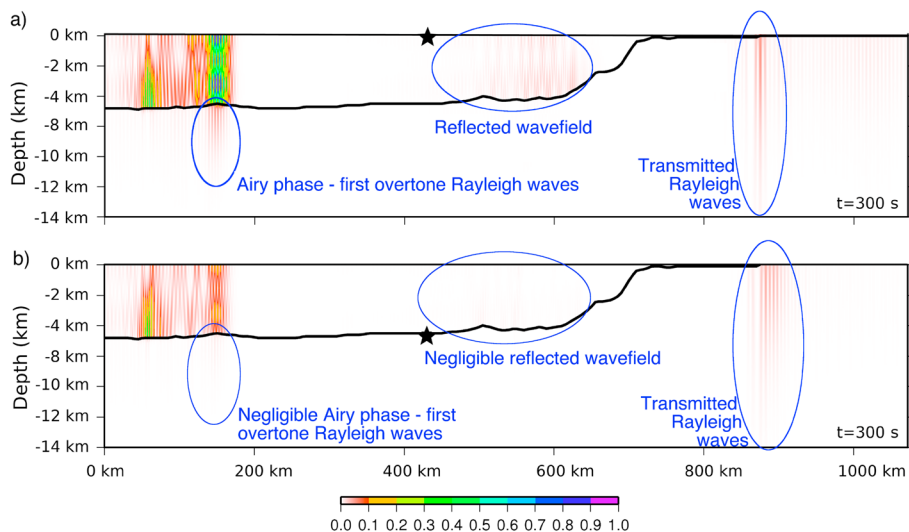


Figure B2. Instantaneous energy at $t = 300$ s associated with the seismic wavefield due to a source located: (a) just below the ocean surface and (b) just below the seafloor. The same seafloor profile has been used in both cases (model b in Figure 1). If the source is located just below the ocean surface (Figure B2a), the reflected instantaneous energy and the amplitude of the first overtone Airy phase (blue ellipses) are stronger than if the source is located below the seafloor (Figure B2b).

The waveform and the relative amplitude of land-recorded seismograms (black traces) are nearly the same in both cases, with Rayleigh waves traveling at about $0.9 \beta_c \approx 3$ km/s.

The main difference is observed on seismograms recorded below the seafloor (blue traces). If the source is located below the seafloor (Figure B1b), in the solid layer, the maximum amplitude is associated with the fast phase of the first overtone of Rayleigh waves, traveling at about 3.2 km/s (seismic phase denoted as phase a in Figure A1). If the source is instead located just below the ocean surface (Figure B1a), in the liquid layer, the maximum amplitude is associated with the Airy phase of the first overtone of Rayleigh waves, which travels at about 1 km/s (seismic phase denoted as phase c in Figure A1).

Figure B2 shows the instantaneous energy at time $t = 300$ s emitted by a source at the ocean surface (Figure B2a) and a source at the ocean seafloor (Figure B2b). The square normalization constants of Figure B1 has been used in order to keep consistency with the synthetic seismograms.

Comparing Figures B2a and B2b, we observe that the land-transmitted energy, associated with the fundamental mode of Rayleigh waves, located between $x = 850$ km and $x = 900$ km, is similarly shaped and its amplitude is characterized by the same order of magnitude in both cases, as already observed in Figure B1 (black traces).

In Figure B2a, around $x = 600$ km, a small amount of energy is reflected back from the ocean-continent boundary. This feature is not present in Figure B2b.

Moreover, in Figure B2a, around $x \approx 150$ km, and below the seafloor we recognize the instantaneous energy associated with the Airy phase of the first overtone (marked by a blue ellipse), which is negligible in Figure B2b.

In this paper a single source has been employed. The differences between the seismic wavefield due to a source at the ocean surface and below the seafloor shown here may be reshaped considering extended sources or grid of point sources, required for modeling seismic noise sources by oceanic storms. Moreover, the presence of a thick sedimentary layer may strongly amplify these differences.

Acknowledgments

Toshiro Tanimoto, Nicholas Harmon, an anonymous reviewer, and the Associate Editor provided many helpful and constructive comments. L.G. thanks Spahr Webb, William Menke, Göran Ekström, Paul G. Richards, and M. Elise Rumpf for stimulating discussions and comments on the manuscript. Comments from Robert Herrmann on the *Computer Program in Seismology* tool and discussions with Fabrice Ardhuin are also gratefully acknowledged. This work was partially supported by the QUEST Initial Training Network funded within the EU Marie Curie Programme. The authors acknowledge the support of the French Agence Nationale de la Recherche (ANR), under the grant ANR-14-CE01-0012 (project MIMOSA). L.G. also acknowledges support from a Lamont-Doherty Earth Observatory Postdoctoral Fellowship and the Brinson Foundation. The 2-D spectral element code used in this study is a modified version of 2DSPEC-2.0 originally developed by G. Festa, E. Delavaud, and J.-P. Vilotte (<http://www.sciences.univ-nantes.fr/lpgnantes/lpg/fichiers/capdeville-y/SPEC2DY0.0.tgz>). Numerical computations were performed on the S-CAPAD platform (IPGP, France) and on the Erdre platform (Centre de Calculs Intensifs des pays de la Loire, France). This is the IPGP contribution 3663.

References

- Aki, K., and P. G. Richards (2009), *Quantitative Seismology*, Univ. Science Books, Sausalito, Calif.
- Ardhuin, F., and T. H. C. Herbers (2013), Noise generation in the solid Earth, oceans and atmosphere, from nonlinear interacting surface gravity waves in finite depth, *J. Fluid Mech.*, **716**, 316–348.
- Ardhuin, F., A. Balanche, E. Stutzmann, and M. Obrebski (2012), From seismic noise to ocean wave parameters: General methods and validation, *J. Geophys. Res.*, **117**, C05002, doi:10.1029/2011JC007449.
- Ardhuin, F., T. Lavanant, M. Obrebski, L. Marié, J.-Y. Royer, J.-F. d'Eu, B. M. Howe, R. Lukas, and J. Aucan (2013), A numerical model for ocean ultra-low frequency noise: Wave-generated acoustic-gravity and Rayleigh modes, *J. Acoust. Soc. Am.*, **134**(4), 3242–3259.
- Ardhuin, F., L. Gualtieri, and E. Stutzmann (2015), How ocean waves rock the Earth: Two mechanisms explain microseisms with periods 3 to 300 s, *Geophys. Res. Lett.*, **42**(3), 765–772, doi:10.1002/2014GL062782.
- Beaudoin, R., and J. Montagner (1996), Time evolution of broadband seismic noise during the french pilot experiment OFM/SISMOBS, *Geophys. Res. Lett.*, **23**(21), 2995–2998.
- Biot, M. (1952), The interaction of rayleigh and stoneley waves in the ocean bottom, *Bull. Seismol. Soc. Am.*, **42**(1), 81–93.
- Bromirski, P. D. (2001), Vibrations from the "Perfect Storm", *Geochem. Geophys. Geosyst.*, **2**(7), 1030, doi:10.1029/2000GC000119.
- Bromirski, P. D., and F. K. Duennebier (2002), The near-coastal microseism spectrum: Spatial and temporal wave climate relationships, *J. Geophys. Res.*, **107**(B8), 2166, doi:10.1029/2001JB000265.
- Bromirski, P. D., R. E. Flick, and N. Graham (1999), Ocean wave height determined from inland seismometer data: Implications for investigating wave climate changes in the NE Pacific, *J. Geophys. Res.*, **104**(C9), 20,753–20,766.
- Bromirski, P. D., F. K. Duennebier, and R. A. Stephen (2005), Mid-ocean microseisms, *Geochem. Geophys. Geosyst.*, **6**, Q04009, doi:10.1029/2004GC000768.
- Bromirski, P. D., R. A. Stephen, and P. Gerstoft (2013), Are deep-ocean-generated surface-wave microseisms observed on land?, *J. Geophys. Res. Solid Earth*, **118**, 3610–3629, doi:10.1002/jgrb.50268.
- Capdeville, Y., and J. J. Marigo (2007), Second order homogenization of the elastic wave equation for non-periodic layered media, *Geophys. J. Int.*, **170**(2), 823–838.
- Cessaro, R. K. (1994), Sources of primary and secondary microseisms, *Bull. Seismol. Soc. Am.*, **84**(1), 142–148.
- Chaljub, E., D. Komatsitsch, Y. Capdeville, J. P. Vilotte, B. Valette, and G. Festa (2007), Spectral-element analysis in seismology, *Adv. Geophys.*, **48**, 365–419.
- Chevrot, S., M. Sylvander, S. Benahmed, C. Ponsolles, J. M. Lefèvre, and D. Paradis (2007), Source locations of secondary microseisms in western Europe: Evidence for both coastal and pelagic sources, *J. Geophys. Res.*, **112**, B11301, doi:10.1029/2007JB005059.
- Collins, J., F. Vernon, J. Orcutt, R. Stephen, K. Peal, F. Wooding, F. Spiess, and J. Hildebrand (2001), Broadband seismology in the oceans: Lessons from the ocean seismic network pilot experiment, *Geophys. Res. Lett.*, **28**(1), 49–52.
- Courant, R., K. Friedrichs, and H. Lewy (1928), Über die partiellen differenzengleichungen der Mathematischen Physik, *Math. Ann.*, **100**(1), 32–74.
- Cupillard, P., E. Delavaud, G. Burgos, G. Festa, J.-P. Vilotte, Y. Capdeville, and J.-P. Montagner (2012), RegSEM: A versatile code based on the spectral element method to compute seismic wave propagation at the regional scale, *Geophys. J. Int.*, **188**(3), 1203–1220.
- Dahlen, F., and J. Tromp (1998), *Theoretical Global Seismology*, Princeton Univ. Press, Princeton, N.J.
- Darbyshire, J. (1992), Microseisms formed off the coast of Norway, *Phys. Earth Planet. Inter.*, **73**(3), 282–289.
- Dziewonski, A. M., and D. L. Anderson (1981), Preliminary reference earth model, *Phys. Earth Planet. Inter.*, **25**(4), 297–356.

- Essen, H.-H., F. Krüger, T. Dahm, and I. Grevemeyer (2003), On the generation of secondary microseisms observed in northern and central Europe, *J. Geophys. Res.*, 108(B10), 2506, doi:10.1029/2002JB002338.
- Ewing, M., W. Jardetzky, and F. Press (1957), *Elastic Waves in Layers Media*, McGraw Hill, New York.
- Festa, G., and J.-P. Vilotte (2005), The newmark scheme as velocity-stress time-staggering: An efficient PML implementation for spectral element simulations of elastodynamics, *Geophys. J. Int.*, 161(3), 789–812.
- Friedrich, A., F. Krüger, and K. Klinge (1998), Ocean-generated microseismic noise located with the Gräfenberg array, *J. Seismol.*, 2(1), 47–64.
- Gerstoft, P., and T. Tanimoto (2007), A year of microseisms in southern California, *Geophys. Res. Lett.*, 34, L20304, doi:10.1029/2007GL031091.
- Gerstoft, P., P. M. Shearer, N. Harmon, and J. Zhang (2008), Global P, PP, and PKP wave microseisms observed from distant storms, *Geophys. Res. Lett.*, 35, L23306, doi:10.1029/2008GL036111.
- Gaultier, L. (2014), Modeling the secondary microseismic noise generation and propagation, PhD thesis, pp. 1–228, Institut de Physique du Globe de Paris (France) and Università di Bologna (Italy).
- Gaultier, L., E. Stutzmann, Y. Capdeville, F. Ardhuin, M. Schimmel, A. Mangeney, and A. Morelli (2013), Modelling secondary microseismic noise by normal mode summation, *Geophys. J. Int.*, 193(3), 1732–1745.
- Gaultier, L., E. Stutzmann, V. Farra, Y. Capdeville, M. Schimmel, F. Ardhuin, and A. Morelli (2014), Modelling the ocean site effect on seismic noise body waves, *Geophys. J. Int.*, 197(2), 1096–1106.
- Harmon, N., D. Forsyth, and S. Webb (2007), Using ambient seismic noise to determine short-period phase velocities and shallow shear velocities in young oceanic lithosphere, *Bull. Seismol. Soc. Am.*, 97(6), 2009–2023.
- Harmon, N., T. Henstock, F. Tilman, A. Rietbrock, and P. Barton (2012), Shear velocity structure across the Sumatran Forearc-Arc, *Geophys. J. Int.*, 189(3), 1306–1314.
- Hasselmann, K. (1963), A statistical analysis of the generation of microseisms, *Rev. Geophys.*, 1(2), 177–210.
- Haubrich, R. A., and K. McCamy (1969), Microseisms: Coastal and pelagic sources, *Rev. Geophys.*, 7(3), 539–571.
- Haxby, W., A. Melkonian, J. Coplan, S. Chan, and W. Ryan (2010), *Geomapapp Freeware Software*, vol. 2.3, Lamont-Doherty Earth Observatory, Palisades.
- Herrmann, R. B. (2013), Computer programs in seismology: An evolving tool for instruction and research, *Seismol. Res. Lett.*, 84(6), 1081–1088.
- Jensen, F. B., W. A. Kuperman, M. B. Porter, and H. Schmidt (2011), *Computational Ocean Acoustics*, Springer Science and Business Media, New York.
- Kedar, S., M. Longuet-Higgins, F. Webb, N. Graham, R. Clayton, and C. Jones (2008), The origin of deep ocean microseisms in the North Atlantic Ocean, *Proc. R. Soc. A*, 464(2091), 777–793.
- Komatitsch, D., S. Tsuboi, and J. Tromp (2005), The spectral-element method in seismology, in *Seismic Earth: Array Analysis of Broadband Seismograms*, vol. 157, edited by A. Levander and G. Nolet, pp. 205–228, AGU, Washington, D. C.
- Koper, K. D., and B. de Foy (2008), Seasonal anisotropy in short-period seismic noise recorded in South Asia, *Bull. Seismol. Soc. Am.*, 98(6), 3033–3045.
- Koper, K. D., B. de Foy, and H. Benz (2009), Composition and variation of noise recorded at the Yellowknife Seismic Array, 1991–2007, *J. Geophys. Res.*, 114, B10310, doi:10.1029/2009JB006307.
- Koper, K. D., K. Seats, and H. Benz (2010), On the composition of Earth's short-period seismic noise field, *Bull. Seismol. Soc. Am.*, 100(2), 606–617.
- Lin, J.-Y., T.-C. Lee, H.-S. Hsieh, Y.-F. Chen, Y.-C. Lin, H.-H. Lee, and Y.-Y. Wen (2014), A study of microseisms induced by Typhoon Nanmadol using ocean-bottom seismometers, *Bull. Seismol. Soc. Am.*, 104(5), 2412–2421.
- Longuet-Higgins, M. S. (1950), A theory of the origin of microseisms, *Philos. Trans. R. Soc. A*, 243, 1–35.
- Maupin, V. (1988), Surface waves across 2-D structures: A method based on coupled local modes, *Geophys. J. Int.*, 93(1), 173–185.
- Nishida, K., H. Kawakatsu, Y. Fukao, and K. Obara (2008), Background Love and Rayleigh waves simultaneously generated at the Pacific Ocean floors, *Geophys. Res. Lett.*, 35, L16307, doi:10.1029/2008GL034753.
- Obrebski, M., F. Ardhuin, E. Stutzmann, and M. Schimmel (2013), Detection of microseismic compressional (P) body waves aided by numerical modeling of oceanic noise sources, *J. Geophys. Res. Solid Earth*, 118, 4312–4324, doi:10.1002/jgrb.50233.
- Obrebski, M. J., F. Ardhuin, E. Stutzmann, and M. Schimmel (2012), How moderate sea states can generate loud seismic noise in the deep ocean, *Geophys. Res. Lett.*, 39, L11601, doi:10.1029/2012GL051896.
- Oliver, J., and M. Ewing (1958), Seismic surface waves at palisades from explosions in Nevada and the Marshall Islands, *Proc. Natl. Acad. Sci.*, 44(8), 780–785.
- Pekeris, C. L. (1948), Theory of propagation of explosive sound in shallow water, *Mem. Geol. Soc. Am.*, 27, 1–116, doi:10.1130/MEM27-2-p1.
- Press, F., and M. Ewing (1948), A theory of microseisms with geologic applications, *Eos Trans. AGU*, 29(2), 163–174.
- Press, F., M. Ewing, and I. Tolstoy (1950), The Airy phase of shallow-focus submarine earthquakes, *Bull. Seismol. Soc. Am.*, 40(2), 111–148.
- Ritzwoller, M. H., and A. L. Levshin (2002), Estimating shallow shear velocities with marine multicomponent seismic data, *Geophysics*, 67, 1991–2004.
- Ryan, W. B., et al. (2009), Global multi-resolution topography synthesis, *Geochem. Geophys. Geosyst.*, 10, Q03014, doi:10.1029/2008GC002332.
- Scholte, J. (1947), The range of existence of rayleigh and stoneley waves, *Geophys. J. Int.*, 5(s5), 120–126.
- Schulte-Pelkum, V., P. S. Earle, and F. L. Vernon (2004), Strong directivity of ocean-generated seismic noise, *Geochem. Geophys. Geosyst.*, 5, Q03004, doi:10.1029/2003GC000520.
- Stehly, L., M. Campillo, and N. M. Shapiro (2006), A study of the seismic noise from its long-range correlation properties, *J. Geophys. Res.*, 111, B10306, doi:10.1029/2005JB004237.
- Stephen, R., P. Bromirski, P. Gerstoft, and P. Worcester (2013), Microseism noise in the Philippine Sea, Abstract S11B-2359 presented at 2013 Fall Meeting, AGU, San Francisco, Calif., 9–13 Dec.
- Stutzmann, E., F. Ardhuin, M. Schimmel, A. Mangeney, and G. Patau (2012), Modelling long-term seismic noise in various environments, *Geophys. J. Int.*, 191(2), 707–722.
- Takeo, A., K. Nishida, T. Isse, H. Kawakatsu, H. Shiobara, H. Sugioka, and T. Kanazawa (2013), Radially anisotropic structure beneath the Shikoku Basin from broadband surface wave analysis of ocean bottom seismometer records, *J. Geophys. Res. Solid Earth*, 118(6), 2878–2892, doi:10.1002/jgrb.50219.
- Takeo, A., D. W. Forsyth, D. S. Weeraratne, and K. Nishida (2014), Estimation of azimuthal anisotropy in the NW Pacific from seismic ambient noise in seafloor records, *Geophys. J. Int.*, 199(1), 11–22.
- Tanimoto, T. (2007), Excitation of microseisms, *Geophys. Res. Lett.*, 34, L05308, doi:10.1029/2006GL029046.
- Tanimoto, T. (2013), Excitation of microseisms: Views from the normal-mode approach, *Geophys. J. Int.*, 194, 1755–1759.

- Tanmoto, T., C. Hadzioannou, H. Igel, J. Wasserman, U. Schreiber, and A. Gebauer (2015), Estimate of Rayleigh-to-Love wave ratio in the secondary microseism by colocated ring laser and seismograph, *Geophys. Res. Lett.*, 42(8), 2650–2655, doi:10.1002/2015GL063637.
- Tian, Y., and M. H. Ritzwoller (2015), Directionality of ambient noise on the Juan de Fuca plate: Implications for source locations of the primary and secondary microseisms, *Geophys. J. Int.*, 201(1), 429–443.
- Webb, S. C. (1998), Broadband seismology and noise under the ocean, *Rev. Geophys.*, 36(1), 105–142.
- Webb, S. C. (2002), Seismic noise on land and on the seafloor, *Int. Geophys.*, 81, 305–318.
- Webb, S. C., and S. C. Constable (1986), Microseism propagation between two sites on the deep seafloor, *Bull. Seismol. Soc. Am.*, 76(5), 1433–1445.
- Woodhouse, J. (1974), Surface waves in a laterally varying layered structure, *Geophys. J. Int.*, 37(3), 461–490.
- Yang, Y., and M. H. Ritzwoller (2008), Characteristics of ambient seismic noise as a source for surface wave tomography, *Geochem. Geophys. Geosyst.*, 9, Q02008, doi:10.1029/2007GC001814.
- Yao, H., P. Gouédard, J. A. Collins, J. J. McGuire, and R. D. van der Hilst (2011), Structure of young East Pacific Rise lithosphere from ambient noise correlation analysis of fundamental-and higher-mode Scholte-Rayleigh waves, *C. R. Geosci.*, 343(8), 571–583.
- Ying, Y., C. J. Bean, and P. D. Bromirski (2014), Propagation of microseisms from the deep ocean to land, *Geophys. Res. Lett.*, 41, 6374–6379, doi:10.1002/2014GL060979.
- Zhang, J., P. Gerstoft, and P. D. Bromirski (2010), Pelagic and coastal sources of *P*-wave microseisms: Generation under tropical cyclones, *Geophys. Res. Lett.*, 37, L15301, doi:10.1029/2010GL044288.